Alkynes in covalent enzyme inhibitors: down the kinetic rabbit hole

Mons, E.

Chapter 5

Covalent EGFR Inhibitors
With a Nonactivated Alkyne Warhead

Mons, E.; Kooij, R.; Sapmaz, A.; Kim, R.Q.; Mulder, M.P.C.; Ovaa, H.

Abstract. Irreversible covalent inhibitors have a crucial role in (receptor) kinase inhibition as they were able to overcome (acquired) resistance to noncovalent inhibitors. Targeted kinase inhibitors (TKIs) covalently target a noncatalytic cysteine thiol at the ATP binding site of the target kinase, that is not present in related kinases. In this work, we investigate if the nonactivated alkyne can be used as a latent electrophile targeting noncatalytic Cys797 in EGFR, as this would reduce the metabolic inactivation and improve the safety profile. To this end, we replaced the acrylamide warhead in approved covalent pan-HER inhibitor **neratinib** (Nerlynx, HKI-272) with a propargylamine (**8RK57**) or 1-amino-3-butyne (**8RK58**). Alkyne-based inhibitors do not exhibit indiscriminate thiol reactivity and potently inhibit EGFR activity, both on recombinant protein as well as in cellular EGFR (auto)phosphorylation assays. Conclusive evidence on a covalent binding mode was not found, and further studies (with alkyne derivatives of other kinase inhibitors) are required to conclude whether the nonactivated alkyne warhead is compatible with kinases such as EGFR, and noncatalytic cysteine thiols in general.

neratinib derivatives — EGFR, Thiol–Alkyne Addition — Covalent adduct with **noncatalytic** Cys797 residue?

1.   Introduction

Many regulatory pathways that keep a cell in check are disrupted in cancer, leading to uncontrollable growth, eventually at the expense of life itself.[1] Traditional cytotoxic chemotherapies cause DNA damage beyond repair thereby inducing cell death, but this is a blunt weapon: all dividing cells will be affected, but cancer cells are affected more because these go through the cell cycle faster (divide more regularly).[2] Personalized or precision medicine is a more selective approach: the genetic or phenotypic tumor profile is used to identify (mutated) proteins or receptors that are (over)expressed in the tumor cells, and treated with targeted therapies that specifically inhibit the function of these oncogenes.[3-4] Tumor cells overexpressing an oncogenic kinase rely on its constitutive kinase activity for survival and/or proliferation – a phenomenon known as oncogene addition – and are disproportionally sensitive to blockage of this signaling: healthy cells express numerous kinases in lower quantities, so their growth and survival is less affected by inhibition of a single kinase.[5-6] This led to the development of orally bioavailable targeted kinase inhibitors (TKIs) that specifically inhibit the activity of important oncogenic (mutant) kinases such as the BCR-Abl fusion protein, the BRAF^{V600E} mutant, and growth factor receptor HER2.[7-10]

Overexpression of epidermal growth factor receptors (ErbB/HER) is associated with malignant phenotypes in several cancer types including breast, non-small cell lung, colorectal and ovarian cancer[11] The HER/ErbB family of RTKs (receptor tyrosine kinases) has four members; EGFR (also known as HER1, ErbB1), HER2 (ErbB2), HER3 (ErbB3) and HER4 (ErbB4) (**Figure 1A**). Growth factor-mediated signal transduction is generally initiated by dimerization of EGFR with another EGFR (homodimerization) or with an ErbB receptor family member (heterodimerization) upon extracellular binding of EGF (epidermal growth factor) or an EGF-like ligand.[11] HER2 – the most oncogenic RTK of the ErbB family – is the favored RTK for EGFR heterodimerization as it does not require ligand-induced conformational change prior to dimerization and has little ability to self-regulate: there is no known growth factor/ligand for HER2.[11-13] An inactive RTK monomer consists of a ligand-binding extracellular domain (ECD), a hydrophobic transmembrane domain, an intracellular tyrosine kinase domain (TKD) and a C-terminal tail (**Figure 1B**). Ligand-mediated receptor dimerization induces intracellular conformational changes in the cytoplasmic tyrosine kinase domain which adopts an active kinase conformation.[14] The active TKD then mediates phosphorylation of specific tyrosine residues on the C-terminal tail of the dimerization partner (*trans*-autophosphorylation), initiating phosphorylation of intracellular signaling kinases thus activating oncogenic downstream signaling pathways implicated in proliferation, survival, adhesion, invasiveness, migration and tumor angiogenesis, eventually leading to tumor growth and survival.[14-15]

Two classes of approved targeted cancer therapies directly interfere with EGFR and/or HER2 signaling: extracellular monoclonal antibodies (mAb) and intracellular targeted kinase inhibitors (TKI) (**Figure 1B**). Monoclonal antibodies are immunoglobulins that bind to the ECD; cetuximab (Erbitux) prevents receptor dimerization by obstructing ligand binding to EGFR,[20-21] trastuzumab (Herceptin) blocks constituent activation and dimerization of HER2,[22] and pertuzumab (Perjeta, 2C4) blocks the dimerization domain of HER2.[23] Antibody therapy is characterized by high target selectivity but is not effective against mutant RTKs that have
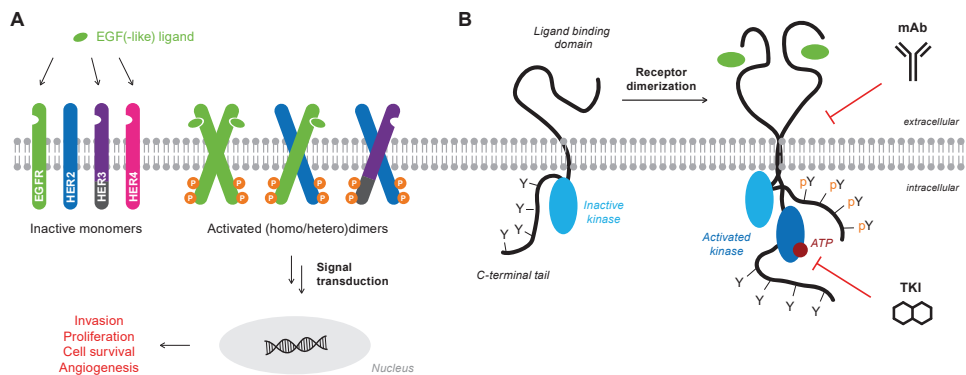
5

Figure 1 | Activation and inhibition of EGFR/HER2-mediated signal transduction. **(A)** Extracellular binding of growth factor to inactive ErbB receptor tyrosine kinase (RTK) monomers promotes receptor (homo/hetero) dimerization, which initiates downstream phosphorylation of an oncogenic signaling cascades eventually leading to tumor growth and survival. HER2 and HER3 are exceptions to this general mechanism; there is no known growth factor/ligand for HER2 (depicted as missing a ligand binding domain) and HER3 is believed to have an inactive "pseudokinase" domain that is not activated upon dimerization (displayed as gray area) but is *trans*-phosphorylated by its heterodimerization partner for cell signaling.[16-17] The HER2/HER3 heterodimer is the most active signaling unit upon neuregulin stimulation, making HER3 the optimal dimerization partner for HER2 despite HER3 not having (significant) kinase activity.[18-19] **(B)** EGFR dimerization induces intracellular conformational changes that activate the kinase domain for *trans*-autophosphorylation of the C-terminal tail. Monoclonal antibodies (mAbs) interfere with the extracellular receptor dimerization/activation while tyrosine kinase inhibitors (TKIs) block ATP binding to the intracellular kinase domain. Adapted from Ferguson.[14]

a consecutively active kinase domain or lack most of the extracellular binding domain; an issue observed with HER2⁺ tumors since the ECD of HER2 is redundant for its activity, and is often cleaved by proteases.[18, 24] TKIs are small molecule inhibitors that bind to the intracellular kinase domain at the ATP-binding site, thereby inhibiting receptor (auto)phosphorylation.[25] HER2-targeting TKIs have a number of advantageous characteristics over the HER2-targeting mAb therapies, such as oral bioavailability – instead of intravenous dosing with mAbs – and their ability to cross the blood-brain barrier required to treat brain metastases that commonly occur in patients with HER2⁺ breast cancer.[24] HER2-targeting TKIs in combination therapy with cytostatic agent capecitabine were found to effectively treat and prevent formation of brain metastases.[26-27] Furthermore, HER2-targeting TKIs directly interfere with kinase activity, thereby retaining activity against the highly active p95HER2 mutant – a truncated form of HER2 that lacks most of the ECD rendering it resistant to mAb therapy (e.g. trastuzumab).[24, 28] To date, noncovalent dual EGFR/HER2 TKI lapatinib (Tykerb, GW572016), noncovalent HER2-selective TKI tucatinib (Tukysa, ONT-380), and covalent pan-HER TKI neratinib (Nerlynx, HKI-272) have been approved for HER2⁺ breast cancer.[29-32]

Initially, the kinase ATP-binding site was considered a poor drug target: TKIs need to overcome competition with 1-5 mM cellular ATP concentrations that greatly exceed the micromolar ATP affinity,[33] and ATP is a substrate for many other kinases and non-kinase proteins, thereby challenging the development of inhibitors selective for a single kinase.[11] Identification of the 4-anilinoquinazoline core significantly improved the potency towards EGFR and led to

the approval of first-generation noncovalent TKIs erlotinib (Tarceva, OSI-774) and gefitinib (Iressa, ZD1839) for treatment of NSCLC (non-small cell lung cancer) (**Figure S1**).[11] However, clinical drug resistance to first-generation TKIs inevitably occurred within 1-2 years after starting therapy,[34-37] because acquired point mutation (T790M) of gatekeeper threonine residue at the ATP-binding site causes steric hindrance while increasing the ATP affinity (**Table S1**, **Table S2**).[38-39] Second-generation TKI afatinib (Gilotrif, BIBW 2992) overcame this resistance by covalent targeting of the exposed thiol side chain of a nonconserved cysteine residue that is uniquely present located at the ATP-binding site of the ErbB/HER family (Cys797 in EGFR, Cys805 in HER2) while not being present in other closely related kinase families.[33, 40-41] Third-generation EGFR TKIs with selectivity for EGFR mutants over EGFR^{WT} have been developed to reduce dose-limiting toxicity – e.g. skin rash and gastrointestinal adverse effects occur at clinically relevant doses for NSCLC treatment – which is associated with concurrent inhibition of EGFR^{WT} in healthy tissue.[25, 39] The mutational burden in HER2-overexpressing breast cancers is lower than in NSCLC, and simultaneous inhibition of EGFR^{WT} (homodimerization) and HER2 (heterodimerization) is an effective strategy.[42-44] Fourth-generation TKIs and combination therapies are currently in (pre)clinical development to overcome the inevitable resistance to covalent TKIs in NSCLC.[25, 34, 40]

The clinical approval of covalent TKIs targeting (mutant) EGFR/HER2 [45-48] and the vast number of covalent TKIs in (clinical) development [49-50] illustrate the success of a covalent binding mode.[7, 41, 51] Irreversible covalent inhibition did not only overcome ATP competition (**Table S2**) but also improved therapeutic efficiency with a prolonged effect long after metabolic clearance since kinase activity is not regained until *de novo* protein synthesis (PK-PD decoupling).[45, 52-53] Safety concerns pertaining the intrinsic ability to form a covalent bond with (nontargeted) thiols no longer automatically eliminate irreversible covalent inhibitors in drug discovery, but low reactivity with nontargeted thiols is desirable nonetheless; adduct formation with biologically relevant thiols reduces the concentration of available unbound inhibitor thereby increasing metabolic clearance and impairing clinical potency.[48]

Targeting EGFR with covalent (nonactivated) alkynes. In our previous work,[54] we demonstrated that the nonactivated alkyne moiety can be employed to covalently target the catalytic cysteine residue of CatK without showing intrinsic reactivity towards nontargeted thiols. In this work, we investigate whether the scope of the nonactivated alkyne warhead can be expanded to TKIs targeting noncatalytic cysteine residues. As a proof-of-concept, we replaced the warhead in covalent pan-HER TKI neratinib [55-56] with a nonactivated alkyne moiety, and evaluated the biochemical potency and binding mode of our analogues.

2. Results and Discussion

Synthesis and design of neratinib analogues. Nonactivated alkyne derivatives were designed with carefully alignment of the reactive alkyne carbon with the reactive acrylamide carbon, by adjusting the linker length (**Figure 2**). The acrylamide warhead of neratinib is introduced in the final synthesis step by reacting 6-amino-quinoline **1** with an acid chloride,[57-59] or at an earlier stage in the synthesis using the same amidation methodology.[56] This synthetic strategy

had to be adjusted to incorporate alkyne warheads connected to the quinoline core through a secondary aniline bond instead of an amide group. Alkyne derivatives 8RK57 and 8RK58 were obtained by treatment of 6-bromoquinoline **2** with propargylamine or 1-amino-3-butyne under Buchwald-Hartwig amination conditions as recommended in the user guide by Surry and Buchwald.[60] A detailed synthetic scheme is provided in **Scheme S1**.

Indiscriminate thiol reactivity. Promiscuous covalent thiol binding of irreversible covalent cysteine-targeting drugs can be assessed with reduced glutathione (GSH) – a naturally occurring tripeptide that traps reactive electrophiles (thus protecting the cell) and is widely used as a benchmark reagent.[61-65] Intrinsic chemical reactivity of (clinical) drug candidates can be assessed by LC-MS detection of unbound inhibitor and covalent inhibitor–thiol adduct upon incubation with a large excess of GSH in aqueous buffer (**Figure 3A**).[63-67] Unbound inhibitor and GSH adduct were quantified from the baseline-separated UV absorbance areas after various incubation times following established protocol.[67] As expected, significant GSH adduct formation was observed with acrylamides afatinib and neratinib but not with noncovalent inhibitor gefitinib nor with alkyne derivatives 8RK57 and 8RK58 (**Figure 3B**).

Covalent EGFR–alkyne adduct is not detected by intact protein MS. Top-down mass spectrometric (MS) analysis of intact protein (adduct) was next performed to evaluate if our alkyne derivatives have a covalent binding mode.[68] Adduct formation of recombinant purified EGFR kinase domain with covalent inhibitors has been reported,[69-70] therefore EGFR (instead of HER2) was selected for MS analysis. Commercially available EGFR kinase domains all had a GST tag (26 kDa), and preliminary MS analysis of unbound recombinant GST-EGFR kinase domain revealed poor ionization and did not form an ionization envelope that could be deconvoluted, possibly related to its large size (>90 kDa) or unfavorable properties of the GST tag (**Figure 4A**).[71-72] An untagged construct of the EGFR kinase domain (695-1022) has previously been used in intact protein MS studies to detect the covalent EGFR–dacomitinib adduct,[69] and the His-tagged version of this construct was indeed compatible with top-down MS (**Figure 4B**). His-EGFR was submitted to LC-MS analysis after incubation with DMSO (unbound) or excess inhibitor for 4 hours. An increase in the deconvoluted mass corresponding with addition of covalent inhibitor was detected upon incubation with covalent inhibitor neratinib, but not with noncovalent inhibitor gefitinib or with alkynes 8RK57 and 8RK58 (**Figure 4B**). Extending the incubation time to 24 hours incubation at room temperature also did not result in detection of a covalent adduct with alkynes 8RK57 and 8RK58 (**Table S4**). Increasing the reaction temperature to speed up the reaction was not a viable strategy as this impaired protein stability and had a detrimental effect on the resolution. Altogether, a covalent EGFR–alkyne adduct was not detected by top-down MS analysis.

Alkynes exhibit tight-binding behavior in a LanthaScreen kinase binding assay. Our efforts shifted to evaluation of biochemical EGFR binding, and whether the alkyne derivatives exhibit time-dependent behavior, as this is a hallmark of (irreversible) covalent inhibition.[52, 75] Considering the dramatic reduction in noncovalent affinity that was observed for alkyne derivatives of ODN,[54] we decided to evaluate EGFR binding potency in the LanthaScreen Eu kinase binding assay: this homogeneous assay is conducted in absence of competing ATP and has successfully been used to evaluate biochemical binding potency and binding reversibility
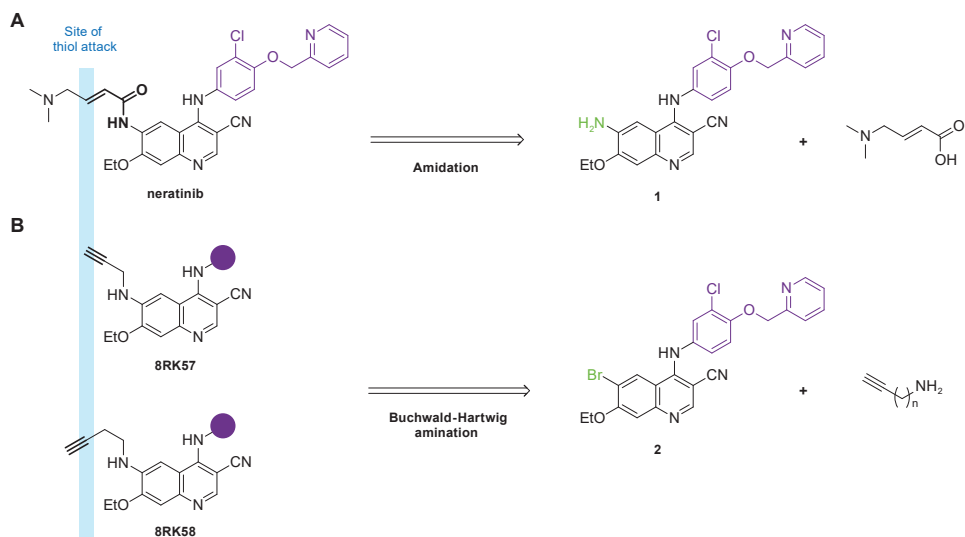
Figure 2 | Synthetic strategy and design of neratinib (derivatives). Alkynes were introduced onto the quinoline core with alignment of the reactive carbon. **(A)** Introduction of acrylamide warhead by late-stage amide coupling. **(B)** Preparation of alkyne derivatives **8RK57** and **8RK58** using Buchwald-Hartwig amination conditions. The 6-bromoquinoline **2** building block was obtained from Mercachem (see also **Scheme S1**).
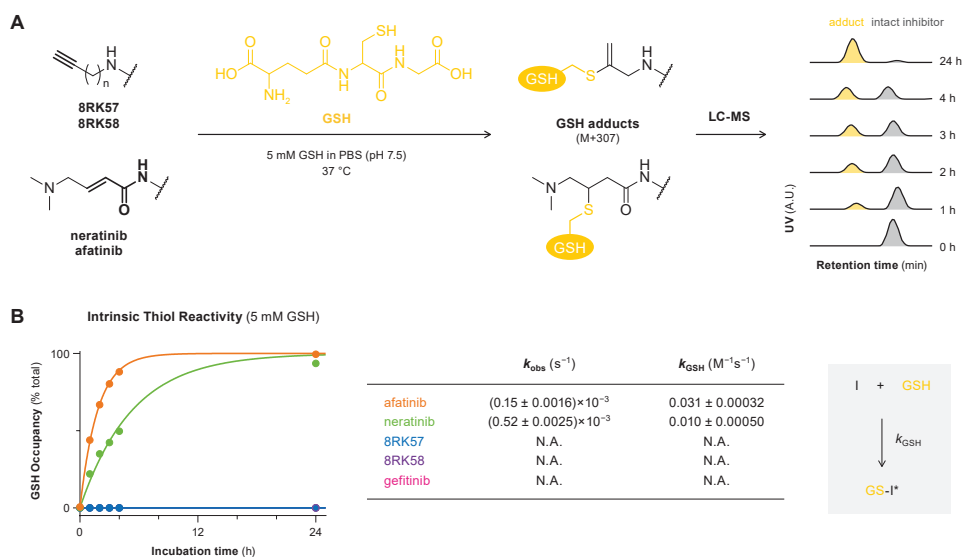
5

Figure 3 | Intrinsic thiol reactivity assessed by LC-MS analysis following established protocol.[54, 67] **(A)** Schematic overview. Parent compound and GSH adduct are quantified from the LC-MS UV trace (λ_{abs} = 350 nm) after incubation with 5 mM GSH. **(B)** Time-dependent GSH adduct formed upon incubation with 5 mM GSH as percentage of total UV area *(left)* and fitted kinetic parameters *(right)*. Values are mean ± SD. k_{GSH} = pseudo-first order reaction rate constant reflecting intrinsic GSH reactivity. Retention times, m/z values and integrated UV areas used for quantification are provided in **Table S3**. Details on calculations of GSH occupancy and fits can be found in *section 4.1*.
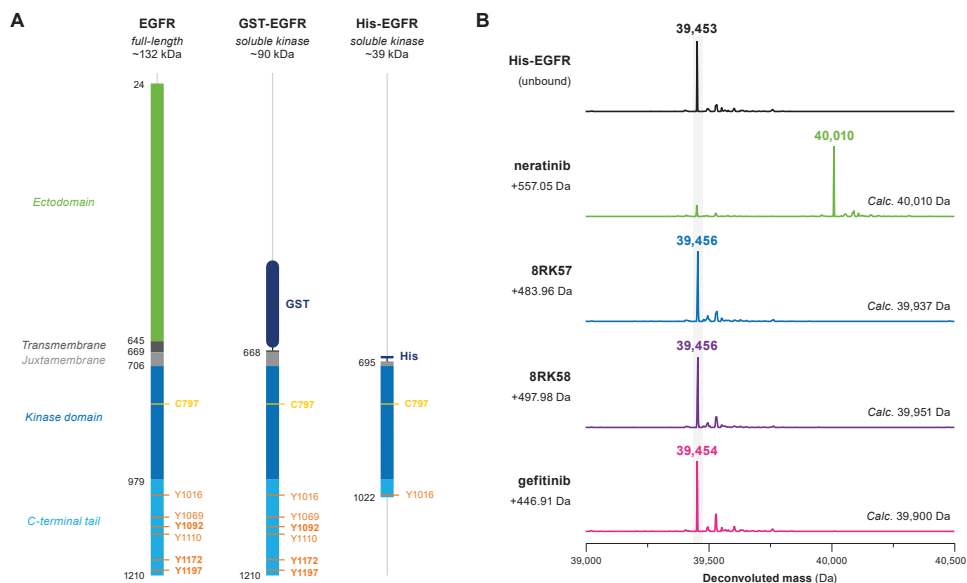
Figure 4 | Direct detection of covalent EGFR–inhibitor adducts by intact protein MS analysis. **(A)** Schematic alignment of full-length EGFR with recombinant kinase domains GST-EGFR and His-EGFR. Adapted from Jura [73] and Cho. [74] EGFR has multiple tyrosine autophosphorylation sites (marked in orange) on its C-terminal tail, which have been omitted in the His-EGFR kinase construct used for intact protein MS analysis. **(B)** Deconvoluted mass of recombinant His-EGFR kinase domain (1 µM) incubated with inhibitor (100 µM) for 4 hours at room temperature. Deconvoluted mass with acrylamide neratinib matches the calculated mass of the covalent adduct, but not for noncovalent inhibitor gefitinib or with alkyne derivatives 8RK57 and 8RK58. Full UPLC traces and ionization envelopes provided in **Figure S2**.

of various kinase inhibitors. [76] EGFR binding potency is detected based on inhibitor-mediated displacement of FRET acceptor tracer 199 (KT199), resulting in a lower FRET signal than in the uninhibited control (**Figure 5A**). [77-78] KT199 consists of FRET acceptor AlexaFluor647 (AF647) conjugated to staurosporine – a known pan-kinase inhibitor that binds at the kinase ATP-binding site (**Figure S3A**, **Table S2**). At a tracer concentration of 25 nM (below the tracer K_M of 45 nM, **Figure S3B**) the TR-FRET originating from the biological binding event was optimally balanced with an acceptable background originating from diffusion-enhanced FRET (**Figure 5B**). To evaluate inhibitor potency of tracer displacement, an adjusted kinetic Probe Competition Assay (kPCA) protocol was employed, following tracer binding in presence of inhibitor after reaction initiation by EGFR addition. [81-82] Neratinib was unable to fully displace the tracer even at concentrations far above its reported potency (IC_{50} = 1 nM), [83] possibly because inhibitor binding does not fully block tracer binding (**Figure 5C**). To our surprise, maximum tracer displacement by 8RK57 and 8RK58 was achieved at reaction initiation, indicative of potent (IC_{50} < 20 nM) binding (**Figure 5C**). This high potency is not indicative of a covalent binding mode: the reported potency of TKIs for the EGFR^{C797S} mutant is in the nM range even though a covalent adduct cannot be formed. [84] Efforts to resolve this tight-binding behavior were unsuccessful (**Figure S3C**). Instead, we evaluated inhibitory potency in an enzymatic activity assay in presence of competing ATP.
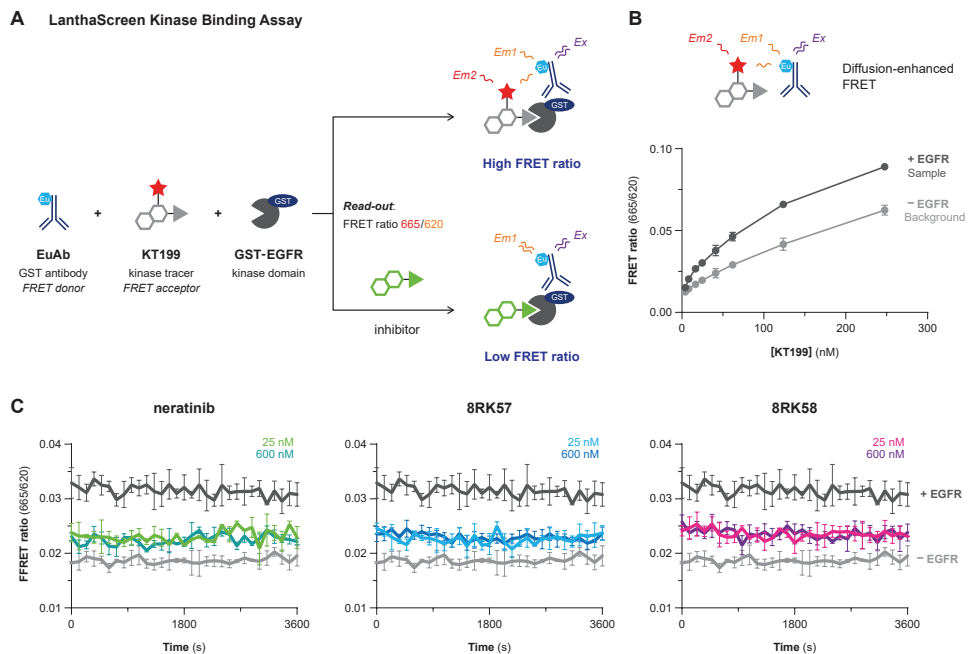
Figure 5 | Biochemical binding potency assessed in a LanthaScreen Eu Kinase Binding Assay. Details on assay optimization are provided in *section 7.5*. **(A)** Assay principle. Upon excitation, Time-Resolved Fluorescence Resonance Energy Transfer (TR-FRET) [79-80] is detected if the FRET donor EuAb (lanthanide Europium (Eu) chelated to an anti-GST antibody) and the FRET acceptor tracer KT199 (AlexaFluor647 conjugated to pan-kinase inhibitor staurosporine, shown in **Figure S3A**) simultaneously bind to the recombinant GST-EGFR kinase domain. KT199 and ATP-competitive inhibitors competitively bind at the kinase ATP binding site, resulting in a dose-dependent decrease of the FRET ratio (acceptor emission/donor emission) as inhibitor outcompetes tracer. **(B)** FRET ratio in absence or presence of EGFR (2 nM) shows tracer-dependent background due to diffusion-enhanced TR-FRET. **(C)** Kinetic probe competition assay (kPCA). Displacement of tracer KT199 (25 nM) by inhibitor (25-600 nM), with reaction initiation by EGFR (2 nM) addition. Maximum tracer displacement was already achieved at reaction initiation.

Alkynes do not exhibit time-dependent behavior in a PhosphoSens kinase activity assay. Most commercial assays to evaluate biochemical kinase inhibition are not compatible with continuous kinetic measurements [85-86] because they require a blocking/quenching/development step prior to read-out for detection of substrate phosphorylation [87] or (^{32}P-labeled) ADP formation/ATP consumption.[88-89] Contrastingly, kinase activity assays based on the Sox technology (PhosphoSens® and its predecessor Omnia®) enable continuous detection of phosphorylation of a Sox-containing peptidic substrate [86, 90-91] in presence of physiological ATP concentrations (1 mM) (**Figure 6A**). This technology is the benchmark method to analyze biochemical potency of covalent clinical candidates,[92-97] and was selected to evaluate inhibitor potency.[98]

An established method based on kinetic measurement of substrate processing under pseudo-first order reaction conditions (see also *Method I* in **Chapter 3**) [99] was employed, thus requiring an absolutely linear curve in the uninhibited sample.[100] Covering the wells with an

5

A **PhosphoSens Kinase Activity Assay**

B

C neratinib / gefitinib / 8RK57 / 8RK58

D

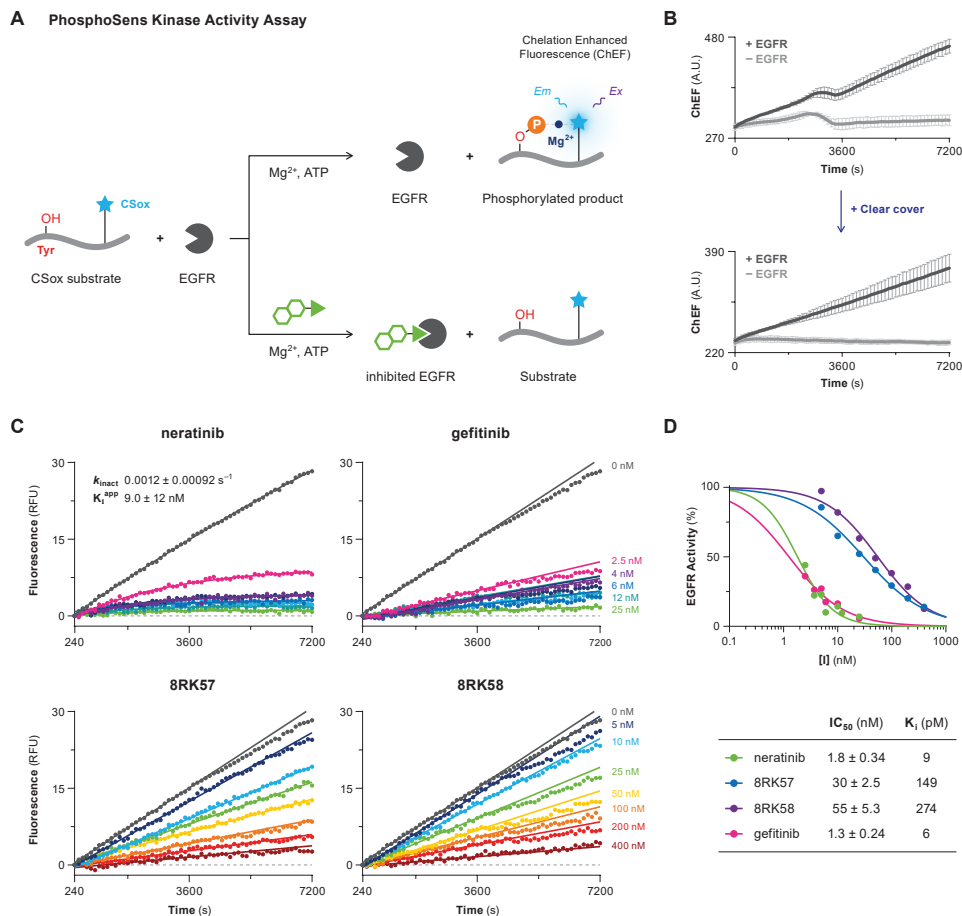|	IC$_{50}$ (nM)	K$_i$ (pM)
neratinib	1.8 ± 0.34	9
8RK57	30 ± 2.5	149
8RK58	55 ± 5.3	274
gefitinib	1.3 ± 0.24	6

Figure 6 | Biochemical EGFR inhibition assessed with PhosphoSens kinase activity assay, in presence of 1 mM ATP. **(A)** Assay principle of the CSox technology for fluorescent kinase activity assays. Phosphorylation of a nearby tyrosine residue increases the Mg^{2+} affinity of the unnatural fluorogenic CSox amino acid, resulting in detection of Chelation-Enhanced Fluorescence (ChEF).[108-109] See also **Figure S4A** for details and structure of the CSox substrate. **(B)** Assay optimization with GST-EGFR kinase domain. Aberrant nonlinearity incompatible with progress curve analysis *(top)* was resolved by covering the wells with a clear adhesive cover *(bottom)*. **(C)** Progress curves for CSox substrate phosphorylation initiated by GST-EGFR (0.25 nM) addition, with kinetic competitive association of 2.5-25 nM (gefitinib, neratinib) or 5-400 nM (8RK57, 8RK58) inhibitor. The first 4 min were omitted to correct for a lag in EGFR activity (more details in *section 7.6*). **(D)** Dose-response curves for EGFR phosphorylation assay in presence of 1 mM ATP. IC$_{50}$ values represent mean ± standard deviation. Inhibitory constant K$_i$ calculated based on reported K$_{M,ATP}$ = 5 μM for EGFR^{WT}.[110]

optical clear cover, per recommendation by the supplier to prevent 'drift'[101] surprisingly also resolved the aberrant nonlinearity observed in the kinetic progress curves of CSox substrate phosphorylation in absence and presence of EGFR kinase domain (**Figure 6B**). This aberrant nonlinearity is not a unique property related to Chelation-Enhanced Fluorescence (λ_{ex} = 360 nm, λ_{em} = 492 nm): we previously observed a similar effect in kinetic assays with detection of fluorescent AMC (λ_{ex} = 350 nm, λ_{em} = 440 nm), Rho110-Gly (λ_{ex} = 487 nm, λ_{em} = 535 nm),

and Rhodol (λ_{ex} = 490 nm, λ_{em} = 545 nm) *(unpublished data)*. Optimization of assay conditions is further discussed in *section 7.6*. EGFR activity in presence of covalent inhibitor neratinib exhibited a clear time-dependence (**Figure 6C**), with kinetic parameters in agreement with reported values.[93] Desired EGFR reactivity – reflected in k_{inact}/K_I – is several magnitudes bigger than the thiol reactivity reflected in k_{GSH} (**Figure 3B**).[102] Time-dependence was not observed for noncovalent inhibitor gefitinib or alkyne derivatives 8RK57 and 8RK58, so their potency for EGFR inhibition is reflected in the equilibrium IC_{50}, which was in the nM range (in presence of 1 mM ATP) (**Figure 6D**).

Irreversible inhibition of cellular EGFR (auto)phosphorylation. Inhibition of cellular EGFR (auto)phosphorylation was evaluated with EGFR activity assays in intact HeLa cells [103-104] – a cervical cancer cell line expressing EGFR and HER2 (HER2$^+$, EGFR$^+$) [105-106] without surface expression of HER3.[107] Briefly, HeLa cells starved of nutrients were incubated with 1 μM inhibitor, optionally followed by treatment with EGF to stimulate receptor (auto)phosphorylation, followed by immunoblotting for EGFR and phosphorylated tyrosine (pY). Visual inspection of the blots indicates that all tested inhibitors inhibited EGFR (auto)phosphorylation at this concentration (**Figure 7A**). Inhibitor reversibility was evaluated in a washout experiment: after incubation with inhibitor (and optionally EGF stimulation), culture medium was replaced by inhibitor-free medium and cells were incubated for another hour (**Figure 7B**). This washout removes unbound inhibitor and stimulates dissociation of reversibly bound inhibitors, thus resulting in higher levels of phosphorylated EGFR for reversible inhibitors while inhibition is retained for inhibitors with an irreversible covalent binding mode. In samples that were not stimulated with EGF (**Figure 7C**, *left*), increased EGFR phosphorylation was indeed observed for reversible inhibitor gefitinib while irreversible inhibitors afatinib and neratinib continued to block receptor (auto)phosphorylation. Surprisingly, EGFR phosphorylation levels with 8RK57 or 8RK58 were not significantly affected by the washout, indicative of an irreversible binding mode. A clear increase in EGFR phosphorylation was observed for all inhibitors in the EGF-stimulated samples after washout (**Figure 7C**, *right*). This can be attributed to *de novo* expression of active EGFR protein during the 1 hour incubation with EGF following inhibitor depletion: EGF stimulation in cell culture promotes lysosomal degradation of internalized EGFR, resulting in a much shorter metabolic half-life of EGFR in presence of EGF (t½ = 1.5 h) than in absence of EGF (t½ = 6.5 h).[111] A preliminary dose-response experiment with EGF-stimulated HeLa cells resulted in a cellular potency of 2 nM for neratinib (**Figure 7D**) – similar to the reported inhibitory potency for (auto)phosphorylation of EGFR (IC_{50} = 3 nM) and HER2 (IC_{50} = 5 nM) in cellular assays on skin cancer cell line A431 (HER2$^+$, EGFR^{+++}) and breast cancer cell line BT474 (HER2^{+++}, EGFR$^+$).[112] Alkyne derivatives 8RK57 and 8RK58 are >20-fold less potent than neratinib, in line with our findings in the kinase activity assay on recombinant GST-EGFR kinase domain (see **Figure 6D**). Interestingly, the IC_{50} of 30 nM for gefitinib is much higher than its potency on recombinant EGFR. This may be attributed to the low HER2 inhibitory potency of gefitinib (see **Table S2**) as EGFR phosphorylation is detected using a general phosphorylated tyrosine (pY) antibody: phosphorylated HER2 (136 kDa) and phosphorylated EGFR (132 kDa) run at a similar height on gel, which 'contaminates' the results. To validate this hypothesis, follow-up experiments with an EGFR-selective phosphotyrosine antibody are required.

5

A EGFR (auto)phosphorylation in HeLa cells

B EGFR (auto)phosphorylation after washout

C EGFR (auto)phosphorylation in HeLa cells

D Cellular potency

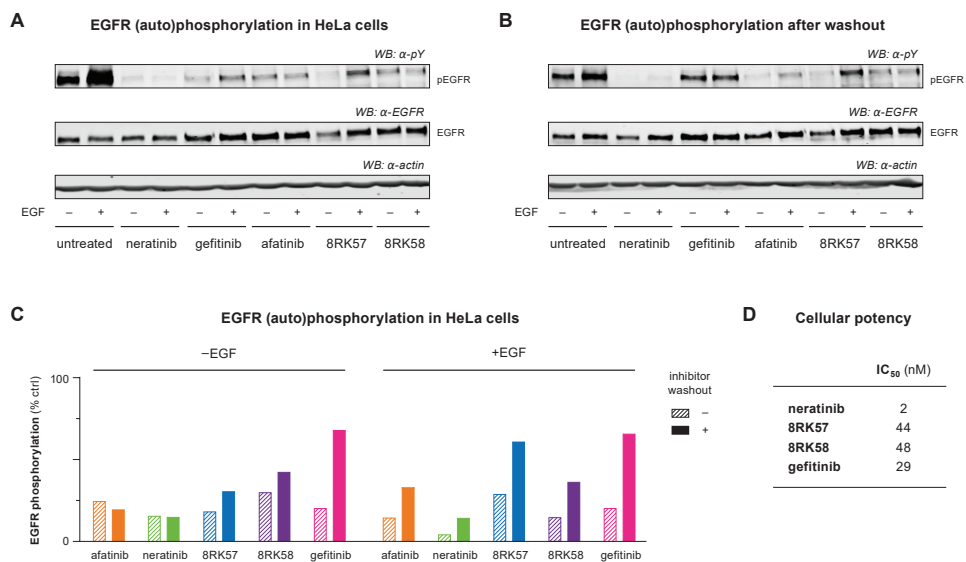|	IC$_{50}$ (nM)
neratinib	2
8RK57	44
8RK58	48
gefitinib	29

Figure 7 | Cellular EGFR (auto)phosphorylation. Starved HeLa cells are treated with inhibitor, optionally with stimulation of receptor phosphorylation by EGF. Lower intensity of the phosphorylated tyrosine (pY) band relative to the total EGFR band corresponds with inhibition of EGFR (auto)phosphorylation. Darker bands indicate more total EGFR/pY. β-actin is a loading control for total protein loading. **(A)** Immunoblotting for phosphorylated tyrosine pY *(top)* and total EGFR *(middle)* in starved HeLa cells treated with 1 µM inhibitor. **(B)** Reversibility experiment. Immunoblotting for phosphorylated tyrosine pY *(top)* and total EGFR *(middle)* in starved HeLa cells treated with 1 µM inhibitor, followed by inhibitor washout. Regained EGFR (auto)phosphorylation can be observed for reversible inhibitors. **(C)** Quantification of EGFR phosphorylation (data shown in *panel A* and *B*), normalized to the phosphorylation levels in the untreated controls for direct comparison of phosphorylation levels with/without inhibitor washout (n = 1). **(D)** Inhibitory potency for cellular EGFR (auto)phosphorylation. Calculated from EGFR (auto)phosphorylation in EGF-stimulated HeLa cells treated with increasing inhibitor concentrations. Phosphorylation levels are quantified from background-corrected pY and total EGFR levels, and normalized to the uninhibited control (n = 1). Full gel scans and dose-response curves are shown in **Figure S5**.

3.   Conclusion and Outlook

In this work, we replaced the warhead in approved covalent kinase inhibitor neratinib (Nerlynx, HKI-272) with a propargylamine (**8RK57**) or 1-but-3-yne (**8RK58**) warhead to investigate whether nonactivated alkynes can covalently target noncatalytic Cys797 at the EGFR ATP-binding site. Covalent adduct formation with nontargeted thiol GSH was not observed, but intact protein MS analysis with recombinant EGFR indicated that covalent EGFR–alkyne adduct was not formed. Preliminary cellular assays were indicative of an irreversible binding mode but kinase activity assays on recombinant GST-EGFR kinase domain did not support this binding mode: 8RK57 and 8RK58 potently inhibit biochemical EGFR activity but did not exhibit time-dependent behavior. Together, these preliminary results indicate alkyne analogues 8RK57 and 8RK58 do not have a covalent binding mode. This may be attributed to experimental design and practical challenges, incompatibility with the mechanism of the thiol–alkyne reaction, or suboptimal inhibitor design.

We cannot exclude the possibility that 8RK57 and 8RK58 have a covalent binding mode, but that contribution of covalent adduct formation was too slow to have a detectable effect on the inhibitory potency, or that we did not detect the covalent adduct due to practical and experimental factors. The covalent thiol–alkyne reaction with the CatK catalytic cysteine residue was relatively slow,[54] and the reaction with a noncatalytic cysteine is expected to result in slower reaction rates: the nucleophilicity of EGFR noncatalytic Cys797 thiol (pKa ~5.5)[113] is less than catalytic cysteine thiolate (pKa ~4/4.5) – though more nucleophilic than general thiols such as the glutathione thiol (pKa ~8.9).[114-115] Preliminary cellular experiments revealed that 8RK57 and 8RK58 effectively inhibit EGFR (auto)phosphorylation in HeLa cells, which was retained in washout experiments – an encouraging indication that 8RK57 and 8RK58 may have an irreversible binding mode. However, it was not possible to validate inhibitor (ir)reversibility in jump dilution assays with recombinant EGFR as we experienced technical/practical issues with diminishing EGFR activity and stability of recombinant EGFR. Recombinant GST-EGFR was unusually sensitive to freeze-thaw cycles and aliquoting, and loss of EGFR activity in single-use aliquots was inevitable: complete loss of enzymatic activity was observed after two freeze-thaw cycles (in the main stock) which could not be resolved by preparation of aliquots (in PCR tubes) as this also inactivated the enzyme. Further investigations into the stability and catalytic activity of recombinant EGFR constructs are desired.

In line with these findings, it is possible that the recombinant His-EGFR construct used for intact protein MS was in an inactive confirmation: all relevant tyrosines except Y1016 have been trimmed from the C-terminal tail. *In vitro* adduct formation with neratinib is expected to be less affected by subtle conformational changes in the recombinant His-EGFR kinase domain – the electrophilic acrylamide has a high intrinsic thiol reactivity (shown in **Figure 3**) – while this could severely impact the rate of *in situ* thiol–alkyne addition, especially compared to reactivity in a cellular context where the EGFR kinase domain is in an active conformation and has an intact C-terminal tail. This may provide an explanation to the lack of covalent EGFR–alkyne adduct detection but more conclusive evidence on the existence of a covalent adduct might be derived from experiments with native (full-length) EGFR – for example in cellular context using bottom-up MS after enrichment for EGFR, or with inhibitor-derived ABPs (these techniques are further discussed in ***Chapter 2***).[68] Alternatively, 8RK57 and 8RK58 may actually <u>not</u> have a covalent binding mode. Based on the current data, we cannot exclude the possibility that the thiol–alkyne reaction is incompatible with noncatalytic cysteines in kinases such as EGFR because stabilization of a carbanion intermediate in the oxyanion hole (*mechanism D* in ***Chapter 1***) is an essential step in covalent adduct formation. However, alkyne derivatives of other kinase inhibitors should be studied before concluding that nonactivated alkynes are incompatible as latent electrophiles to target noncatalytic cysteine thiols. The design of 8RK57 and 8RK58 may not have facilitated covalent adduct formation: thiol–alkyne adduct formation is a proximity-driven reaction, and suboptimal orientation or juxtaposition of the reactive carbon in the alkyne warhead hampers adduct formation. In ***Chapter 4***,[54] we showed that a small molecule recognition element was sufficient to form a covalent adduct with alkyne **EM04** when we replaced the ODN nitrile group with an isosteric alkyne. To make alkyne analogues of neratinib, we had to replace an acrylamide moiety with a nonactivated alkyne which may have affected the positioning negatively.

5

The reactive warhead in neratinib is a 4-(dimethylamino)crotonamide: the acrylamide is modified with a polar, basic tertiary dimethylamine group on the β-carbon. The dimethylamine moiety improves aqueous solubility, and binding models suggest that it is a directing group that facilitates deprotonation of Cys805 to form the reactive thiolate (**Figure 8A**), thus promoting adduct formation with HER2 while sterically hindering adduct formation with nontargeted thiols.[45, 83, 112] We did not include this directing group in our inhibitor design because it is not essential for the appropriate juxtaposition of the electrophile relative to the nucleophilic EGFR Cys797 thiolate: covalent TKIs including osimertinib (AZD-9292, Tagrisso) and canertinib (CI-1033, PD183805) covalently modify Cys797 without the need for this directing group. However, the dimethylamine group does contribute to potency: Wissner and Mansour[55] report that the cellular EGFR/HER2 potency of acrylamide **6** (PD168393) was lower than its dimethylamine derivative **9a**, and a similar trend was observed for 2-butynamide **7** (CL-387785, EKI-785)[116] and its dimethylamine derivative **10**. Other indications of a beneficial contribution of a directing group are the basic piperidine moiety on the terminal position of approved TKI dacomitinib (PF-00299804, Vizimpro): Wood *et al.*[117] found that introduction of a basic pyrrolidine moiety onto the alkyne warhead increases the rate of EGFR adduct formation with 6-ethynyl-thienopyrimidines. It is worthwhile to investigate if introduction of a basic (tertiary) amine moiety on the terminal position of the nonactivated alkyne promotes covalent EGFR–alkyne adduct formation (**Figure 8B**). Neratinib displays a low off-target reactivity with Src kinase despite sharing the 4-phenylamino-3-quinolinecarbonitrile core with ATP-competitive Src kinase inhibitors,[118] which may be attributed to the 4-(dimethylamino) crotonamide warhead on the quinoline C6 position: introduction of water-solubilizing group on C6 has been reported to mitigate Src kinase inhibition.[119] Nonactivated alkyne derivatives **8RK57** and **8RK58** likely exhibit off-target Src kinase reactivity, which may be mitigated by including a basic solubilizing group on the terminal position.
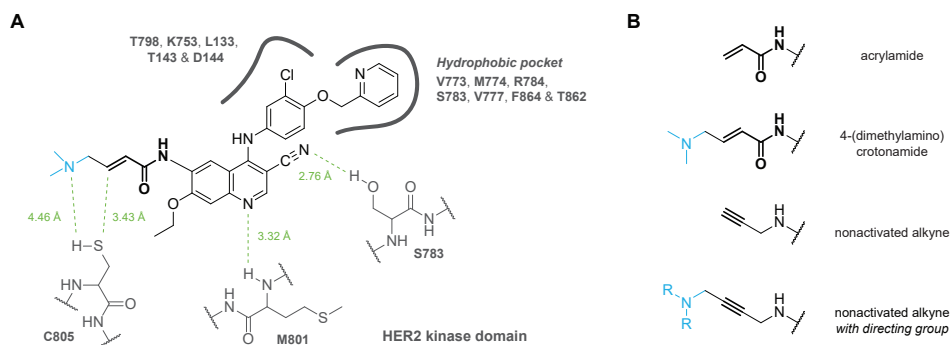

Figure 8 | Role of dimethylamine moiety as directing groups promoting covalent adduct formation. **(A)** Binding model of neratinib with HER2 before covalent adduct formation. Adapted from Tsou *et al.*[56] Introduction of the lipophilic 2-pyridynylmethyl motif improved HER2 potency by occupying a hydrophobic pocket. The basic dimethylamine moiety on the acrylamide warhead promotes adduct formation with HER2 Cys805.[55] **(B)** Structures of acrylamide warhead, 4-(dimethylamino)crotonamide warhead with a dimethylamine directing group on the terminal position, nonactivated alkyne warhead, and proposed nonactivated alkyne warhead with a basic directing group on the terminal position.

To investigate whether the nonactivated alkyne is compatible with kinases – the most prevalent category of irreversible covalent inhibitors – future efforts should be directed towards nonactivated alkyne derivatives of other scaffolds. Here, the focus should be on acrylamides rather than 4-(dimethylamino)crotonamides – these have a higher chance of success because they do not need a directing group – ideally targeting mutant EGFR as assay tools to study mutant EGFR adduct formation are more widely available compared to HER2. In this context, EGFR[T790M]-selective inhibitor osimertinib (AZD-9292, Tagrisso) would be an appropriate model: the acrylamide has successfully been replaced to generate allenamide analogues,[120] indicating a flexibility in warhead architecture. Alternatively, replacing an electron-deficient alkyne with a nonactivated alkyne could be explored, such as the 2-butynamide warhead in 4-anilinopyrido[3,4-d]pyrimidine **29**,[121] or in 4-anilinoquinazoline CL-387785 (EKI-785).[116]

To conclude, we were unable to demonstrate whether the nonactivated alkyne is a suitable latent electrophile for targeting the noncatalytic Cys797 in EGFR kinase. However, this is no definitive evidence that the nonactivated alkynes are unsuitable in general, and they still have a potential role in irreversible covalent TKI development. Future studies should be directed towards modification of the inhibitor scaffold and optimization of the electrophile position relative to the reactive cysteine thiol.

Acknowledgements

Author Contributions

E.M.: Methodology, Investigation *(Chemical Synthesis, Biochemical Assays)*, Writing – Original Draft. R.K.: Investigation *(Chemical Synthesis)*. A.S.: Investigation *(Cellular Assays)*, Writing – Review & Editing. R.Q.K.: Supervision, Writing – Review & Editing. M.P.C.M.: Supervision, Writing – Review & Editing. H.O.: Conceptualization, Supervision.

5

4.   Materials and Methods: *Biochemistry*

General

Reaction buffers are freshly supplemented with DTT (Chem-Impex, #00127), stored in single-use aliquots at −20 °C (1M in water). Established EGFR TKIs neratinib (Adv. ChemBlocks, #10409) and afatinib are taken along as irreversible covalent inhibitor controls, and gefitinib (SigmaAldrich, #SML1657) as reversible noncovalent inhibitor control. Purified recombinant human EGFR (UniProtID: P00533) kinase domains used in this work can be found below.

Enzyme	Tag	Domain	Source or reference
His-EGFR	His	CD^{WT} (695-1022)	*In-house*. This work
GST-EGFR	GST	CD^{WT} (668-1210)	ThermoFisher, #PV3872
GST-EGFR	GST	CD^{WT} (668-1210)	SignalChem, #E10-112G

4.1. Intrinsic Thiol Reactivity Assay

A reaction mixture containing inhibitor (100 µM) and GSH (5 mM) in PBS (10 mM phosphate buffer pH7.45, 140 mM NaCl, 2.7 mM KCl) was incubated at 37 °C under gentle agitation (300 rpm) for the indicated incubation time (0/1/2/3/4/24 h) after which a sample (25 µL) was removed. The samples were quenched by 2-fold diluted in 0.1% FA (aq) and submitted to LC-MS analysis. Chromatographic separation and MS analysis (10 µL injection) was carried out on a Waters ACQUITY UPLC H-class System equipped with Waters ACQUITY Quaternary Solvent Manager (QSM), Waters ACQUITY UPLC Photodiode Array (PDA) eλ Detector (λ = 210-800 nm), Waters ACQUITY UPLC BEH C18 Column (300 Å, 1.7 µm, 2.1×50 mm) and LCT Premier Orthogonal Acceleration Time of Flight Mass Spectrometer (m/z = 100-1600) in ES+ mode. Samples were run with a 1.6 min 2-100% gradient (run time 3 min) using 96% water and 96% MeCN mixed with 2.5% FA in water/MeCN as mobile phases (flow rate = 0.5 mL/min). Data processing was performed using Waters MassLynx Mass Spectrometry Software V4.2. Time-dependent unreacted inhibitor and GSH adduct signal in each sample was quantified from the baseline-separated UV absorbance peak area at a fixed wavelength (λ_{abs} = 350 nm) using the MassLynx Integrated peaks functionality. Data were plotted and analyzed using GraphPad Prism 8.4.2. Graphical data represents mean ± standard error obtained for a single representative experiment from fitting biological duplicates (n = 2).

The GSH occupancy was calculated by dividing the integrated UV area of GSH adduct over the integrated UV area of GSH adduct and unbound inhibitor, and normalized to 100%.

$$\text{GSH Occupancy} \ = \ 100\% \ \frac{\text{UV}_{\text{adduct}}}{\left(\text{UV}_{\text{adduct}} + \text{UV}_{\text{inhibitor}}\right)}$$

Time-dependent GSH occupancy (% of total) was plotted against incubation time for each inhibitor and fitted to the exponential one-phase association equation below (GraphPad Prism: One-phase association, with restrained values Y0 = 0% and plateau = 100%) to obtain rate of adduct formation k_{obs} in presence of 5 mM GSH.

$$\left(\text{GSH Occupancy}\right)_t \ = \ 100\% \ \left(1 - e^{-k_{obs}t}\right)$$

Observed rate k_{obs} was then used to calculate the pseudo-first order rate constant k_{GSH} reflecting the intrinsic GSH reactivity. The standard deviation σ of k_{GSH} was calculated with Gaussian error propagation.

$$k_{\text{GSH}} \ = \ \frac{k_{obs}}{[\text{GSH}]} \quad with \quad \sigma_{k_{\text{GSH}}} = \frac{\sigma_{k_{obs}}}{[\text{GSH}]}$$

4.2. Protein Expression and Purification

Human EGFR (residues 695-1022) was cloned into baculovirus shuttle vector pNKI2.13 harboring an N-terminal His-tag and a 3C protease site using LIC cloning.[122] The construct was sequence-verified before transposition into baculovirus vector (Bacmid) using DH10Bac cells. His-EGFR was expressed using baculovirus expression in Spodoptera frugiperda (Sf9) using an adapted Bac-to-Bac system (Invitrogen). Bacmids were isolated from DH10Bac cells using isopropanol precipitation and 10 µg was transfected into $0.8×10^6$ sedentary Sf9 cells using CellFectin (Invitrogen) in SFM-II medium (Gibco) in a 6-well plate at 28 °C. After 72 h cells were checked for swelling and the medium was harvested (P0) for infection of P1 cultures; 50 mL of $1×10^6$ cells/mL in SFM-II medium. P1 cultures were incubated at 28 °C whilst shaking for 72 h and then harvested by spinning down at 500 G for 5 min. The supernatant was used to infect P2 cultures (like P1, but now 500 mL), whilst the pellet was used to check for expression and purification optimization. P2 cultures were infected with low MOI and harvested after 72 h shaking at 28 °C. Cell pellets were dissolved in buffer A (50 mM Tris pH8.0, 150 mM NaCl, 5 mM β-mercaptoethanol (BME)) and disrupted using sonication before centrifugation at 24,000 G for 40 min at 4 °C. The supernatant was applied to a 1 mL HisTrap column (GE Healthcare) using buffer A and the protein was eluted using a gradient of buffer B (Buffer A supplemented with 500 mM imidazole). Protein-containing fractions

were pooled, concentrated and applied to gel filtration on a Superdex 200 column (GE Healthcare) in a Tris buffer (20 mM Tris pH8.0, 150 mM NaCl, and 5 mM BME). The protein fractions were concentrated to 2.7 mg/mL before being aliquoted and flash-frozen using liquid nitrogen.

4.3.   Intact Protein MS

Recombinant His-tagged EGFR kinase domain (1 μM) and inhibitor (100 μM) were incubated in reaction buffer (50 mM HEPES pH7.4, 150 mM NaCl and 5 mM DTT) at 21 °C for 4 h in Protein Lobind Tubes (Eppendorf, #022431018) prior to LC-MS analysis. Chromatographic separation and MS analysis (1 μL injection) was carried out on a Waters ACQUITY UPLC-MS system equipped with a Waters ACQUITY Quaternary Solvent Manager (QSM), Waters ACQUITY FTN AutoSampler, Waters ACQUITY UPLC Protein BEH C4 Column (300 Å, 1.7 μm, 2.1×50 mm) and XEVO-G2XS QTOF Mass Spectrometer (m/z = 200-2500) in ES+ mode. Samples were run with a 6 min 18-50% gradient (run time 15 min) using 0.1% FA in MeCN and 0.1% FA in water as mobile phases (flow rate 0.6-0.8 mL/min). The first 4 min the flow (2% solvent B) was diverted to the waste to avoid contamination of the MS with high concentrations of buffer components. After 4 min, the elution flow was ionized with an electrospray ionization (ESI) source in positive ion mode. The data was analyzed using Waters MassLynx Mass Spectrometry Software V4.2. The total mass of the covalent EGFR−inhibitor adducts was obtained by deconvolution of electrospray ionization mass spectrum envelope (average isotopes) with the MaxEnt1 function. Sample carry-over was minimized by running wash runs (run time 3 min) with 80% MeOH in water (5 μL injection, twice) and 60% MeCN in water (5 μL injection, twice) after each sample.

4.4.   LanthaScreen Eu Kinase Binding Assay

Inhibitor binding to recombinant GST-tagged EGFR kinase domain (ThermoFisher, #PV3872) was assessed in a LanthaScreen Eu Kinase Binding Assay with TR-FRET signal between acceptor Kinase Tracer 199 (KT199; ThermoFisher, #PV5830) and donor LanthaScreen Eu-anti-GST Antibody (ThermoFisher, #PV5594) as read-out.[78] Assay components were diluted in 1× Kinase Buffer A (50 mM HEPES pH7.5, 10 mM MgCl$_2$, 1 mM EGTA, 0.01% Brij-35) freshly prepared from Invitrogen 5× Kinase Buffer A (ThermoFisher, #PV3189). LanthaScreen Eu-anti-GST Antibody was thawed, mixed and centrifuged (10,000 rpm, 10 min) prior to pipetting from the top of the solution and dilution into reaction buffer to prevent artefacts caused by solid particles. A stock solution containing GST-EGFR and anti-GST EuAb was preincubated for at least 30 min prior to addition (to reach the slow EGFR−EuAb equilibrium).

Inhibitors (10-100 μM in DMSO) and KT199 (25 μM in DMSO) were transferred to PE OptiPlate-384 White Microplates (PerkinElmer, #6007290) or Corning 4513 White Low Volume NBS 384 Well Microplates (Corning, #4513) using an ECHO 550 Liquid Handler (Labcyte Inc.) acoustic dispenser. Time resolved fluorescence (TRF) of the Eu-labeled donor (λ_{ex} = 337 nm, λ_{em} = 620 ± 10 nm) and AlexaFluor647-labeled acceptor (λ_{em} = 665 ± 10 nm) was measured in relative fluorescence units (RFU) on a CLARIOstar (BMG Labtech) microplate reader in well multichromatics mode (Excitation filter: EX TR. Dichroic filter: LP TR. 100 flashes/well. 100 μs delay before integration start. 200 μs integration time). The ratiomeric TR-FRET emission of acceptor over donor ($TRF_{665\,nm}/TRF_{620\,nm}$) was calculated from individual donor/acceptor TRF emission intensities with MARS Data Analysis Software (BMG Labtech). All measurements were performed in triplicate unless otherwise noted. Data were plotted and analyzed using GraphPad Prism 8.4.2. Graphical data represents the mean ± standard deviation for a single representative experiment.

Tracer dissociation constant K$_D$. 5-300 nL KT199 (25 μM in DMSO, with DMSO backfill to 300 nL) was dispensed into an PE OptiPlate-384 microplate using an ECHO acoustic dispenser. Then, 30 μL of preincubated 1× EGFR/EuAb solution (final concentration 2 nM EGFR, 0.5 nM EuAb) or 30 μL of 1× EuAb solution (final concentration 0.5 nM) was added. The plate was shaken to mix (600 rpm, 1 min) and centrifuged (1000 rpm, 1 min). Time Resolved Fluorescence (TRF) was measured every 2 min for 60 min. Background in absence of EGFR (diffusion-enhanced FRET and nonspecific binding) was subtracted from the FRET ratio in presence of EGFR. The

corrected FRET ratio (after 20 min incubation, at equilibrium) was plotted against tracer concentration and fitted to the quadratic equation below with fixed values for $[E]_0$ (EGFR concentration at reaction initiation) and $[L]_0$ (tracer concentration at reaction initiation) to determine tracer binding affinity K_D accounting for ligand depletion ($[tracer]_0 < 10[EGFR]_0$).

$$FRET_{sample}^{corr} = B_{max} \frac{([E]_0 + [L]_0 + K_D) - \sqrt{([E]_0 + [L]_0 + K_D)^2 - 4[E]_0[L]_0}}{2[E]_0}$$

Kinetic Probe Competition Assay (kPCA). 0-270 nL inhibitor (DMSO backfill to 270 nL) and 30 nL KT199 (25 µM in DMSO, final concentration 25 nM) were dispensed into an PE OptiPlate-384 microplate using an ECHO acoustic dispenser. Then, 4 µL Kinase Buffer A was added to each well, the plate was shaken to mix (300 rpm, 1 min) and centrifuged (1000 rpm, 1 min). Finally, 26 µL of the preincubated 1.2× EGFR/EuAb solution (final concentration 2 nM EGFR, 0.5 nM EuAb) or 26 µL of 1.2× EuAb solution (final concentration 0.5 nM) was added and the plate was centrifuged (1000 rpm, 1 min). Time Resolved Fluorescence (TRF) was measured every 2 min for 60 min.

4.5. PhosphoSens Protein Kinase Activity Assay

Biochemical inhibition of recombinant EGFR kinase domain (ThermoFisher, #PV3872 or SignalChem, #E10-112G) was assessed in a PhosphoSens Protein Kinase Activity Assay (AssayQuant, #CSKS-AQT0734K) with Chelation-Enhanced Fluorescence (ChEF) upon CSox substrate phosphorylation as read-out. Assay components were stored as stock solutions at −20 °C as recommended by supplier.[101] Dry powder stock of PhosphoSens CSox substrate (AssayQuant, #CSKS-AQT0734B) was dissolved in 20% NH_4CO_3 (aq) to a concentration of 1 mM and diluted in distilled water. Single-use aliquots of DTT (100 mM in water) and ATP (100 mM in water) were stored at −20 °C. Buffers were freshly supplemented with EGTA, DTT and ATP before use. Single-use aliquots of purified recombinant human GST-EGFR kinase domain were diluted with enzyme buffer (20 mM HEPES pH7.5, 0.01% Brij-35, 5% Glycerol, 1 mg/mL BSA, 0.1 mM EGTA and 1.0 mM DTT) in Protein Lobind Tubes (Eppendorf, #022431018) to minimize loss of enzyme activity due to precipitation/aggregation. Stock solution of 12.5 µM CSox substrate AQT734 (AssayQuant, #AQT0734B) was prepared in reaction buffer (62.5 mM HEPES pH7.5, 0.01% Brij-35, 12.5 mM $MgCl_2$, 0.69 mM EGTA, 1.25 mM DTT and 1.25 mM ATP). The final buffer composition in each well was 54 mM HEPES, 0.012% Brij-35, 1% Glycerol, 0.20 mg/mL BSA, 0.6 mM EGTA, 10 mM $MgCl_2$, 1 mM ATP and 1.2 mM DTT.

Kinetic Competitive Association. 0-200 nL inhibitor (100× in DMSO, DMSO backfill to 200 nL) was transferred to Corning 3820 Black Low Volume NBS 384 Well Microplates (Corning, #3820) using an ECHO 550 Liquid Handler (Labcyte Inc.) acoustic dispenser, followed by addition of 16 µL CSox substrate AQT734 (1.25× in reaction buffer, 10 µM final concentration) to each well. The plate was shaken to mix (300 rpm, 1 min) before addition of 4 µL GST-EGFR (5× in enzyme buffer, 0.25 nM final concentration) or 4 µL enzyme buffer (no kinase control). The plate was centrifuged at 1,000 rpm for 1 min and the wells were sealed with clear tape (Duck® Brand HP260™ Packing Tape) applied with a roller prior to minimize assay artefacts such as drift due to evaporation. Chelation-Enhanced Fluorescence intensity ($\lambda_{ex} = 360 \pm 15$ nm, $\lambda_{em} = 492 \pm 20$ nm) was measured every 2 min for 120 min on a CLARIOstar (BMG Labtech) microplate reader. All measurements were performed in triplicate. Data were plotted and analyzed using GraphPad Prism 8.4.2. Background fluorescence (time-dependent fluorescence intensity for CSox substrate in absence of EGFR) was subtracted from the time-dependent fluorescence intensities in presence of EGFR (and inhibitor) (GraphPad Prism: Remove Baseline and Column Math – Value-Baseline with Baseline = Selected Column). Values in the lag phase (0-4 min) were excluded before baseline removal to correct for compound fluorescence (GraphPad Prism: Remove Baseline and Column Math – Value-Baseline with Baseline = First Row), to give the corrected fluorescence intensity (in RFU). Graphical data represents the mean ± standard deviation for a single representative experiment.

Data Analysis: Progress Curve Analysis. Corrected ChEF (in RFU) was plotted against incubation time (in s) for each inhibitor concentration, and fitted to the one-phase exponential association equation below to obtain the rate constant k_{obs} (in s^{-1}) for time-dependent formation of fluorescent phosphorylated CSox product. Lag time was constrained to t_{lag} = 240 s and final velocity v_s was constrained to v_s = 0 for irreversible inhibitor neratinib. The progress curve of the uninhibited DMSO control was also fitted to find k_{ctrl}.

$$F_t = v_s(t - t_{lag}) + \frac{v_i - v_s}{k_{obs}} \left[1 - e^{-k_{obs}(t - t_{lag})} \right] + F_0$$

For irreversible inhibitor neratinib, the means and standard errors of k_{obs} (in s^{-1}) were plotted against inhibitor concentration (in M), and fitted to the equation below to obtain maximum inactivation rate constant k_{inact} (in s^{-1}) and apparent inactivation constant K_I^{app} (in M) in presence of 1 mM ATP. Nonlinearity in uninhibited k_{ctrl} was constrained to the k_{obs} of the uninhibited control.

$$k_{obs} = k_{ctrl} + \frac{k_{inact}[I]}{K_I^{app} + [I]}$$

Data Analysis: Equilibrium Potency. Corrected fluorescence intensity (in RFU) was plotted against incubation time (in s) for each inhibitor concentration, and fitted to a straight line to calculate the phosphorylation velocity v (slope in RFU/s) during the first 4-60 min. The mean and standard error were plotted against inhibitor concentration and fitted to the nonlinear least squares curve equation (GraphPad Prism: [Inhibitor] vs. response – Variable slope (four parameters)) with fixed values for the top (v^{max}, uninhibited control) and bottom (v^{min} = 0) to obtain IC$_{50}$-values reflecting biochemical inhibitory potency in presence of 1 mM ATP.

$$v = v^{min} + \frac{v^{max} - v^{min}}{1 + \left(\frac{IC_{50}}{[I]} \right)^h}$$

Biochemical potency K_i of ATP-competitive reversible inhibitors was obtained using the Cheng-Prusoff equation below. The $K_{M,ATP}$ value for EGFR^{WT} ATP affinity was constrained to the reported $K_{M,ATP}$ = 5 µM.[110]

$$K_i = \frac{IC_{50}}{\left(1 + \frac{[ATP]}{K_{M,ATP}} \right)}$$

4.6. Cellular EGFR Inhibition and Reversibility Assay

HeLa cells were cultured in DMEM (Dulbecco's Modified Eagle's Medium, Gibco) supplemented with 7.5% FCS. Cells were maintained in a humidified atmosphere of 5% CO$_2$ at 37 °C and regularly tested for the absence of mycoplasma.

Cellular EGFR (auto)phosphorylation

Inhibition. HeLa cells were seeded into 12 well plates (8×10^4 cells/well) and incubated overnight. Medium was changed to serum-free DMEM to starve the cells, and cells were grown for 2 h. DMSO or inhibitor (1 µM) was added to the serum-free medium and incubated for 1 h. For EGF stimulated samples, 25 ng/mL EGF (Gibco, #PHG0313) was added and cells were incubated for 1 h (after incubation with inhibitor). Medium was removed and plates were stored at −80 °C until the next day. EGFR (auto)phosphorylation was visualized by gel electrophoresis and immunoblotting (see below).

Reversibility/washout. Culturing and treatment of HeLa cells as described for the inhibition assay above. Following inhibitor incubation, medium was replaced by fresh, inhibitor-free medium (optionally containing 25 ng/mL EGF) to evaluate reversibility.

Cellular inhibitory potency. Culturing and treatment of HeLa cells as described for the inhibition assay above, with incubation with DMSO or inhibitor (0-2 µM), followed by stimulation with EGF. EGFR phosphorylation was visualized and quantified as described below (n = 1). Receptor phosphorylation was plotted against inhibitor concentration, and fitted to obtain IC_{50}-values using non-linear least squares curve fitting (GraphPad Prism: [inhibitor] vs. response – variable slop (four parameters)) with fixed values for the top (100%) and bottom (0%).

Gel Electrophoresis and Western Blotting. 50 µL of 2× SDS sample buffer containing 20 mM DTT (Invitrogen, #N0007) was added to each well and incubated at 37 °C. Proteins from the whole cell lysate (WCL) were denatured by heating at 100 °C for at least 15 min. Samples (25 µL) were loaded on 8% Tris-glycine SDS-PAGE gels and resolved by gel electrophoresis. Proteins were transferred to a nitrocellulose membrane (Protan BA85, 0.45 µm, GE Healthcare) at 300 mA for 2.5 h using a Trans-Blot Turbo Transfer System (Biorad). The membranes were blocked in blocking buffer (5% skim milk powder (Oxiod, #LP0031) in PBS (Sigma-Aldrich, #P1379)) for 1 h. Antibodies were prepared in 5% milk in PBST (0.1% Tween20 in PBS). Primary antibodies: rabbit anti-EGFR (1:1,000; Millipore, #04-338), mouse anti-phosphotyrosine clone 4G10 (1:1,000; Millipore, #05-321), and mouse anti-β-actin clone AC-74 (1:10,000; Sigma-Aldrich, #A2228). Secondary antibodies: IRDye 800CW goat anti-mouse (1:5,000; Li-COR, #926-32210) and IRDye 680LT goat anti-rabbit (1:20,000; Li-COR, #926-68021). The membranes were incubated with a primary antibody, washed three times for 10 min in 0.1% PBST, incubated with the secondary antibody for 30 min, and washed three times again in 0.1% PBST. The signal was detected using direct imaging by the Odyssey Classic imager (LI-COR).

Quantification. Intensity of signals corresponding to total EGFR and phosphorylated EGFR in the pY blot were quantified with ImageJ v1.52a,[123-125] and the gel-specific background was subtracted. Relative receptor phosphorylation (pY/EGFR) was calculated for each sample and then normalized to the maximum receptor phosphorylation, corresponding to pY/EGFR in the respective controls: vehicle-treated samples +/− EGF stimulation, +/− washout. Data were plotted and analyzed using GraphPad Prism 8.

5.   Materials and Methods: *Chemical Synthesis*

The synthetic strategy for preparation of **8RK57** and **8RK58** can be found in **Scheme S1**. Chemical synthesis of precursor bromoquinoline **2** was performed at Mercachem BV (Nijmegen, NL). Synthesis of alkyne derivatives 8RK57 and 8RK58 was performed at LUMC (Leiden, NL).

General. All commercially available reagents and solvents were used as purchased, including BrettPhos Palladacycle G3 (Strem Chemicals, #46-0322) and BrettPhos (Strem Chemicals, #15-1152). Reported yields are not optimized. Thin Layer Chromatography (TLC) was performed using TLC plates from Merck (SiO_2, Kieselgel 60 F254 neutral, on aluminum with fluorescence indicator) and compounds were visualized by UV detection (254 nm) and $KMnO_4$ staining. Flash column chromatography (FCC) purification of precursors **2-5** was performed using the indicated eluent. FCC purification of **8RK57** and **8RK58** was performed using Grace Davisil Silica Gel (particle size 40-63 µm, pore diameter 60 Å) and the indicated eluent. Nuclear magnetic resonance (NMR) spectra were recorded as indicated on a Bruker Avance 300 (300 MHz for ^{1}H and 75.00 MHz for ^{13}C) instrument or a Bruker Avance 600 (600 MHz for ^{1}H and 151 MHz for ^{13}C) instrument equipped with a Bruker CryoPlatform using the residual solvent (DMSO-d_6) as internal standard (δ 2.50 ppm for ^{1}H and δ 39.52 ppm for ^{13}C). Chemical shifts (δ) are given in ppm and coupling constants (*J*) are quoted in hertz (Hz). Resonances are described as s (singlet), d (doublet), t (triplet), q (quartet), b (broad) and m (multiplet) or combinations thereof. Assignment of signals is based on 2D NMR techniques COSY, HSQC and HMBC. High-resolution mass spectrometry (HRMS) measurements were carried out on a Waters ACQUITY UPLC-MS system equipped with a Waters ACQUITY

Quaternary Solvent Manager (QSM), Waters ACQUITY FTN AutoSampler, Waters ACQUITY UPLC BEH C18 Column (1.7 µm, 2.1×50 mm) and XEVO-G2 XS QTOF Mass Spectrometer (m/z = 50-1200) in ES+ mode. Samples were run with a 1.7 min gradient (run time 3 min) using 0.1% FA in MeCN and 0.1% FA in water as mobile phases (flow rate 0.6 mL/min). The elution flow was ionized with an electrospray ionization (ESI) source in positive ion mode. Data processing was performed using Waters MassLynx Mass Spectrometry Software 4.2. Mass spectra were centered to obtain the found mass with the TOF spectrum center function; Process – Center – Half height = 2, Center method = Median. Theoretical mass was calculated with the isotope modelling function; Tools – Isotope model – Charged ion – Charge state = 1.

LC-MS Method I. LC-MS analysis of precursors **3-5** was performed at Mercachem (Nijmegen, NL) on a system equipped with a Diode Array (DAD) Detector (λ = 220-320 nm), Waters XSelect C18 Column (3.5 µm, 2.1×30 mm), an Electron-Spray Atmospheric Pressure Ionization (ES-API) source and a (MSD) Mass Spectrometer (m/z = 100-800) in ESI+ mode. Samples were run with a linear 1.6 min gradient (run time 3 min) of 5-98% solvent A, using A = 95% MeCN + 5% $(NH_4)HCO_3$ (aq) and B = 10 mM $(NH_4)HCO_3$ in water (pH9.0) as mobile phases (flow rate = 1.0 mL/min).

LC-MS Method II. LC-MS analysis of precursor **2** and final compounds **8RK57** and **8RK58** was performed at LUMC (Leiden, NL) on a Waters ACQUITY UPLC H-class System equipped with Waters ACQUITY Quaternary Solvent Manager (QSM), Waters ACQUITY UPLC Photodiode Array (PDA) eλ Detector (λ = 210-800 nm), Waters ACQUITY UPLC BEH C18 Column (130 Å, 1.7 µm, 2.1×50 mm) and LCT Premier Orthogonal Acceleration Time of Flight Mass Spectrometer (m/z = 100-1600) in ES+ mode. Pure compounds were run with a 7 min 2-100% gradient (run time 10 min) using 96% water and 96% MeCN mixed with 2.5% FA in water/MeCN as mobile phases (flow rate = 0.5 mL/min).

## 5.1.   Synthesis of Precursor 2

3-chloro-4-(2-pyridylmethoxy)aniline **5**
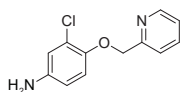
Following published procedure,[126] 4-amino-2-chlorophenol **6** (5.00 gr, 34.8 mmol, 1.0 eq) was reacted with 2-(chloromethyl)pyridine hydrochloride (6.86 gr, 41.8 mmol, 1.2 eq) in presence of benzaldehyde (3.88 mL, 38.3 mmol, 1.1 eq) and K_2CO_3 (19.25 gr, 139 mmol, 4 eq) in 40 mL DMF, at 50 °C for 24 h. The mixture was concentrated *in vacuo* and carefully dissolved (gas evolution) in 300 mL 2N HCl. The aqueous solution was extracted with EtOAc (3X) and basified by addition of 300 mL 2N NaOH. The resulting suspension was stirred, filtered and thoroughly washed with water. The brownish residue was taken up in EtOAc, washed with water and brine, dried over Na_2SO_4 and concentrated *in vacuo* to give aniline **5** as a light-brown solid (7.46 gr, 29.6 mmol, 85%). The material was used in the next step without further purification. LC-MS (ESI+); Rt = 1.88 min, m/z = 235 [M+H]+.

*N-(3-chloro-4-(2-pyridinemethoxy)phenyl)-2-cyanoacetamide* **4**
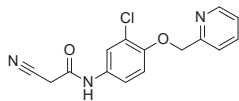
A solution of aniline **5** (2.00 gr, 8.52 mmol, 1 eq) and 2-cyanoacetic acid (761 mg, 8.95 mmol, 1.05 eq) in 30 mL anhydrous THF was heated at reflux, and *N,N'*-diisopropylcarbodiimide (1.39 mL, 8.95 mmol, 1.05 eq) was added dropwise. The resulting mixture was heated at reflux for 1 h. Reaction progress monitored by LC-MS revealed full conversion, and the reaction mixture was cooled to room temperature and concentrated *in vacuo*. The reaction mixture was suspended in 30 mL EtOAc, stirred overnight at room temperature, filtered and dried. LC-MS analysis of the residue revealed contamination with diisopropyl urea, which was removed by coating on Hydromix and purification by FCC (gradient 0-10% MeOH in EtOAc), followed by coating on silica and purification by FCC (gradient 5-10% MeOH in EtOAc) to obtain acetamide **4** as a white solid (1.69 gr, 5.32 mmol, 62.4%). Spectral ^{1}H NMR data of acetamide **4** is in agreement with published data.[57] LC-MS (ESI+); Rt = 1.92 min, m/z = 302 [M+H]+.

(E/Z)-3-(4-bromo-3-ethoxyanilino)-N-[3-chloro-4-(2-pyridinyl-methoxy)phenyl]-2-cyano-2-propenamide **3**
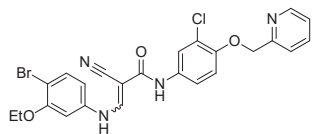
Adapted from published procedure,[127] acetamide **4** (1.00 gr, 3.31 mmol, 1 eq) and 4-bromo-3-ethoxyaniline hydrochloride **7** (837 mg, 3.31 mmol, 1 eq) were suspended in 30 mL iPrOH. Triethyl orthoformate (0.55 mL, 3.31 mmol, 1 eq) was added and the mixture was heated to reflux. Another equivalent of triethyl orthoformate (0.55 mL, 3.31 mmol, 1 eq) was added 1.5 hours and 3.5 hours after reaction initiation. LC-MS analysis revealed incomplete conversion (60%) therefore additional triethyl orthoformate (1.1 mL, 6.6 mmol, 2 eq) was added and reflux was continued for a further 4 hours, but this did not significantly improve conversion. Additional 4-bromo-3-ethoxyaniline hydrochloride **7** (418 mg, 1.66 mmol, 0.5 eq) and 4 mL iPrOH were added and the mixture was refluxed overnight. Reaction conversion was still incomplete (80%), therefore additional 4-bromo-3-ethoxyaniline hydrochloride **7** (418 mg, 1.66 mmol, 0.5 eq) was added and the mixture was refluxed overnight. The reaction mixture was allowed to cool to room temperature, filtered and dried when consumption of starting material was >90%. The product was obtained by trituration from 20 mL iPrOH. Cyanoacrylamide (E/Z)-**3** was obtained as a cream solid (1.31 gr, 2.14 mmol, 65%) and used in the next step without further purification (78% major isomer, 8.3% minor isomer and 11% starting material). LC-MS (ESI⁺); Rt = 2.41 min, m/z = 527 & 529 [M+H]⁺ *(major)* + Rt = 2.28 min, m/z = 527 & 529 [M+H]⁺ *(minor)*.

6-bromo-4-((3-chloro-4-(pyridin-2-ylmethoxy)phenyl)amino)-7-ethoxyquinoline-3-carbonitrile **2**
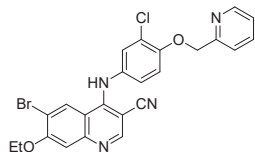
Adapted from published procedure,[127] cyanoacrylamide (E/Z)-**3** (1.31 gr, 2.48 mmol, 1 eq) was suspended in 15 mL anhydrous toluene. Pyridine (0.40 mL, 4.96 mmol, 2 eq) was added and the mixture was heated to reflux. Phosphorus(V) oxychloride (0.46 mL, 4.96 mmol, 2 eq) was added and the mixture refluxed for 1 h. The reaction mixture was concentrated *in vacuo* and resuspended in a mixture of EtOAc/MeOH and 2N NaOH (aq). The aqueous phase was extracted with EtOAc twice, and the combined organic layers were washed with water, brine, dried over Na₂SO₄ and concentrated *in vacuo*. The material was coated on silica and purified by FCC (gradient 80-100% EtOAc in heptane). Fractions containing product were pooled and concentrated to afford 6-bromo-4-anilino-3-quinolinecarbonitrile **2** (0.46 gr, 0.866 mmol, 35%) as an orange-yellow solid. TLC Rf = 0.44 (3:1 EtOAc/heptane). LC-MS (ESI⁺); Rt = 4.62 min, m/z = 509.0 & 511.0 [M+H]⁺. ¹H NMR (600 MHz, DMSO-d_6) δ 9.75 (s, 1H), 8.78 (s, 1H), 8.60 (dt, *J* = 4.8, 1.3 Hz, 1H), 8.52 (s, 1H), 7.88 (td, *J* = 7.7, 1.8 Hz, 1H), 7.58 (d, *J* = 7.8 Hz, 1H), 7.47 (d, *J* = 2.2 Hz, 1H), 7.40 (s, 1H), 7.37 (ddd, *J* = 7.6, 4.8, 1.1 Hz, 1H), 7.28 (d, *J* = 8.8 Hz, 1H), 7.26 (dd, *J* = 8.8, 2.2 Hz, 1H), 5.30 (s, 2H), 4.29 (q, *J* = 6.9 Hz, 2H), 1.44 (t, *J* = 6.9 Hz, 3H). ¹³C NMR DEPTQ135 (151 MHz, DMSO-d_6) δ 156.91, 156.10, 154.04, 151.86, 150.39, 149.84, 149.16, 137.11, 132.78, 127.18, 127.11, 125.53, 123.10, 121.48, 121.46, 116.88, 114.19, 113.77, 112.43, 109.93, 86.18, 71.18, 65.03, 14.32. HRMS (ESI⁺): calculated 509.0380 & 511.0360 for C₂₄H₁₈N₄O₂BrCl ([M+H]⁺), found: 509.0381 & 511.0364.

5.2. Synthesis of 8RK57 and 8RK58

General Procedure A: Buchwald-Hartwig Amination

6-bromoquinoline **2** (50 mg, 0.098 mmol, 1 eq), BrettPhos Palladacycle G3 (35.56 mg, 0.039 mmol, 0.4 eq), BrettPhos (21.06 mg, 0.039 mmol, 0.4 eq) and NaOtBu (28.28 mg, 0.29 mmol, 3 eq) were combined in a flame-dried Schlenk flask under argon, to which anhydrous DMF (5 mL) was added. Finally, primary amine (0.98 mmol, 10 eq) was added, and the reaction mixture was stirred overnight at 70 °C. Reaction progress was monitored by TLC and LC-MS (detection of unreacted 6-bromoquinoline **2**). Upon reaction completion the reaction mixture was coated on silica and separated by FCC (gradient 0-100% EtOAc in heptane). Fractions containing desired product were pooled and solvent was removed by rotary evaporation. The product was lyophilized to obtain product as a dry powder.

4-((3-chloro-4-(pyridin-2-ylmethoxy)phenyl)amino)-7-ethoxy-6-(prop-2-yn-1-ylamino)quinoline-3-carbonitrile
8RK57
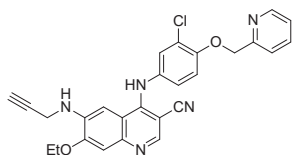
Following *general procedure A*, Buchwald-Hartwig amination with propargylamine (63 μL, 0.98 mmol, 10 eq) afforded alkyne **8RK57** as a yellow powder (17 mg, 0.035 mmol, 36%). TLC Rf = 0.49 (4:1 EtOAc/heptane). LC-MS (ESI+); Rt = 3.97 min, m/z = 484.1 [M+H]+. ^{1}H NMR (300 MHz, DMSO-d_6) δ 9.30 (s, 1H), 8.60 (ddd, J = 4.9, 1.8, 0.9 Hz, 1H), 8.34 (s, 1H), 7.88 (td, J = 7.7, 1.8 Hz, 1H), 7.58 (dt, J = 7.8, 1.1 Hz, 1H), 7.41 (d, J = 2.4 Hz, 1H), 7.37 (ddd, J = 7.6, 4.8, 0.8 Hz, 1H), 7.28 (s, 1H), 7.27 (d, J = 8.7 Hz, 1H), 7.21 (dd, J = 8.8, 2.5 Hz, 1H), 7.20 (s, 1H), 6.05 (t, J = 6.4 Hz, 1H), 5.29 (s, 2H), 4.25 (q, J = 6.9 Hz, 2H), 4.07 (dd, J = 6.4, 2.4 Hz, 2H), 3.04 (t, J = 2.3 Hz, 1H), 1.45 (t, J = 6.9 Hz, 3H). ^{13}C NMR APT (75 MHz, DMSO-d_6) δ 156.17, 151.36, 151.15, 149.15, 148.88, 148.23, 143.22, 137.71, 137.10, 134.02, 126.26, 124.52, 123.09, 121.54, 121.47, 117.42, 114.35, 114.19, 106.93, 97.88, 86.95, 81.65, 73.01, 71.21, 64.18, 31.83, 14.40. HRMS (ESI+): calculated 484.1540 for $C_{27}H_{22}N_5O_2Cl$ ([M+H]+), found: 484.1537.

6-(but-3-yn-1-ylamino)-4-((3-chloro-4-(pyridin-2-ylmethoxy)phenyl)amino)-7-ethoxyquinoline-3-carbonitrile
8RK58
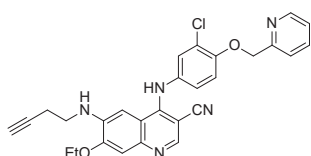
Following *general procedure A*, Buchwald-Hartwig amination with 1-amino-3-butyne (80 μL, 0.98 mmol, 10 eq) afforded alkyne **8RK58** as a yellow powder (29 mg, 0.058 mmol, 59%). TLC Rf = 0.33 (3:1 EtOAc/heptane). LC-MS (ESI+); Rt = 4.23 min, m/z = 498.2 [M+H]+. ^{1}H NMR (300 MHz, DMSO-d_6) δ 9.36 (s, 1H), 8.60 (ddd, J = 4.9, 1.8, 1.0 Hz, 1H), 8.33 (s, 1H), 7.87 (td, J = 7.7, 1.8 Hz, 1H), 7.58 (dt, J = 7.9, 1.1 Hz, 1H), 7.42 (d, J = 2.4 Hz, 1H), 7.37 (ddd, J = 7.6, 4.8, 1.2 Hz, 1H), 7.27 (d, J = 8.9 Hz, 1H), 7.21 (dd, J = 9.0, 2.8 Hz, 1H), 7.20 (s, 1H), 7.19 (s, 1H), 5.71 (t, J = 6.1 Hz, 1H), 5.30 (s, 2H), 4.25 (q, J = 6.9 Hz, 2H), 3.40 (q, J = 7.0 Hz, 2H), 2.90 (t, J = 2.6 Hz, 1H), 2.54 (td, J = 7.3, 2.7 Hz, 2H), 1.45 (t, J = 6.9 Hz, 3H). ^{13}C NMR APT (75 MHz, DMSO-d_6) δ 156.16, 151.34, 151.11, 149.16, 148.97, 147.81, 142.45, 138.42, 137.10, 133.90, 126.61, 124.89, 123.09, 121.54, 121.48, 117.32, 114.33, 114.30, 106.65, 96.66, 86.78, 82.58, 72.54, 71.22, 64.23, 41.46, 18.01, 14.39. HRMS (ESI+): calculated 498.1697 for $C_{28}H_{24}N_5O_2Cl$ ([M+H]+), found: 498.1695.

6. References

1. Mukherjee, S. *The Emperor of All Maladies: A Biography of Cancer.* Scribner: New York, U.S.A., 2010.

2. Tilsed, C.M.; Fisher, S.A.; Nowak, A.K.; Lake, R.A.; Lesterhuis, W.J. Cancer Chemotherapy: Insights into Cellular and Tumor Microenvironmental Mechanisms of Action. *Front. Oncol.* **2022**, *12*, 960317. doi: 10.3389/fonc.2022.960317.

3. Gambardella, V.; Tarazona, N.; Cejalvo, J.M.; Lombardi, P.; Huerta, M.; Roselló, S.; Fleitas, T.; Roda, D.; Cervantes, A. Personalized Medicine: Recent Progress in Cancer Therapy. *Cancers* **2020**, *12*, 1009. doi: 10.3390/cancers12041009.

4. Schirrmacher, V. From Chemotherapy to Biological Therapy: A Review of Novel Concepts to Reduce the Side Effects of Systemic Cancer Treatment. *Int. J. Oncol.* **2019**, *54*, 407-419. doi: 10.3892/ijo.2018.4661.

5. Carey, L.A. HER2—A Good Addiction. *Nat. Rev. Clin. Oncol.* **2012**, *9*, 196-197. doi: 10.1038/nrclinonc.2012.36.

6. Sharma, S.V.; Settleman, J. Oncogene Addiction: Setting the Stage for Molecularly Targeted Cancer Therapy. *Genes Dev.* **2007**, *21*, 3214-3231. doi: 10.1101/gad.1609907.

7. Roskoski, R. Orally Effective FDA-Approved Protein Kinase Targeted Covalent Inhibitors (TCIs). *Pharmacol. Res.* **2021**, *165*, 105422. doi: 10.1016/j.phrs.2021.105422.

8. Zhang, J.; Yang, P.L.; Gray, N.S. Targeting Cancer with Small Molecule Kinase Inhibitors. *Nat. Rev. Cancer* **2009**, *9*, 28-39. doi: 10.1038/nrc2559.

9. Proietti, I.; Skroza, N.; Michelini, S.; Mambrin, A.; Balduzzi, V.; Bernardini, N.; Marchesiello, A.; Tolino, E.; Volpe, S.; Maddalena, P.; Di Fraia, M.; Mangino, G.; Romeo, G.; Potenza, C. BRAF Inhibitors: Molecular Targeting and Immunomodulatory Actions. *Cancers* **2020**, *12*, 1823. doi: 10.3390/cancers12071823.

10. Lovly, C.M.; Shaw, A.T. Molecular Pathways: Resistance to Kinase Inhibitors and Implications for Therapeutic Strategies. *Clin. Cancer Res.* **2014**, *20*, 2249-2256. doi: 10.1158/1078-0432.Ccr-13-1610.

11. Roskoski, R. The ErbB/HER Receptor Protein-Tyrosine Kinases and Cancer. *Biochem. Biophys. Res. Commun.* **2004**, *319*, 1-11. doi: 10.1016/j.bbrc.2004.04.150.

12. Pohlmann, P.R.; Mayer, I.A.; Mernaugh, R. Resistance to Trastuzumab in Breast Cancer. *Clin. Cancer Res.* **2009**, *15*, 7479. doi: 10.1158/1078-0432.CCR-09-0636.

5

13. Arkhipov, A.; Shan, Y.; Kim, E.T.; Dror, R.O.; Shaw, D.E. Her2 Activation Mechanism Reflects Evolutionary Preservation of Asymmetric Ectodomain Dimers in the Human EGFR Family. *eLife* **2013**, *2*, e00708. doi: 10.7554/eLife.00708.

14. Ferguson, K.M. Structure-Based View of Epidermal Growth Factor Receptor Regulation. *Annu. Rev. Biophys.* **2008**, *37*, 353-373. doi: 10.1146/annurev.biophys.37.032807.125829.

15. Díaz-Serrano, A.; Gella, P.; Jiménez, E.; Zugazagoitia, J.; Paz-Ares Rodríguez, L. Targeting EGFR in Lung Cancer: Current Standards and Developments. *Drugs* **2018**, *78*, 893-911. doi: 10.1007/s40265-018-0916-4.

16. Shi, F.; Telesco, S.E.; Liu, Y.; Radhakrishnan, R.; Lemmon, M.A. ErbB3/HER3 Intracellular Domain Is Competent to Bind ATP and Catalyze Autophosphorylation. *Proc. Natl. Acad. Sci.* **2010**, *107*, 7692. doi: 10.1073/pnas.1002753107.

17. van Lengerich, B.; Agnew, C.; Puchner, E.M.; Huang, B.; Jura, N. EGF and NRG Induce Phosphorylation of HER3/ERBB3 by EGFR Using Distinct Oligomeric Mechanisms. *Proc. Natl. Acad. Sci.* **2017**, *114*, E2836-E2845. doi: 10.1073/pnas.1617994114.

18. Arkin, M.; Moasser, M.M. HER2 Directed Small Molecule Antagonists. *Curr. Opin. Investig. Drugs* **2008**, *9*, 1264-1276.

19. Tzahar, E.; Waterman, H.; Chen, X.; Levkowitz, G.; Karunagaran, D.; Lavi, S.; Ratzkin, B.J.; Yarden, Y. A Hierarchical Network of Interreceptor Interactions Determines Signal Transduction by Neu Differentiation Factor/Neuregulin and Epidermal Growth Factor. *Mol. Cell. Biol.* **1996**, *16*, 5276-5287. doi: 10.1128/MCB.16.10.5276.

20. Ciardiello, F.; Tortora, G. EGFR Antagonists in Cancer Treatment. *N. Engl. J. Med.* **2008**, *358*, 1160-1174. doi: 10.1056/NEJMra0707704.

21. Voigt, M.; Braig, F.; Göthel, M.; Schulte, A.; Lamszus, K.; Bokemeyer, C.; Binder, M. Functional Dissection of the Epidermal Growth Factor Receptor Epitopes Targeted by Panitumumab and Cetuximab. *Neoplasia* **2012**, *14*, 1023-1031. doi: 10.1593/neo.121242.

22. Okines, A. F. C.; Cunningham, D. Trastuzumab: A Novel Standard Option for Patients with HER-2-Positive Advanced Gastric or Gastro-Oesophageal Junction Cancer. *Ther. Adv. Gastroenterol.* **2012**, *5*, 301-318. doi: 10.1177/1756283X12450246.

23. Bonello, M.; Sims, A.H.; Langdon, S.P. Human Epidermal Growth Factor Receptor Targeted Inhibitors for the Treatment of Ovarian Cancer. *Cancer Biol. Med.* **2018**, *15*, 375-388. doi: 10.20892/j.issn.2095-3941.2018.0062.

24. Collins, D.M.; Conlon, N.T.; Kannan, S.; Verma, C.S.; Eli, L.D.; Lalani, A.S.; Crown, J. Preclinical Characteristics of the Irreversible Pan-HER Kinase Inhibitor Neratinib Compared with Lapatinib: Implications for the Treatment of HER2-Positive and *HER2*-Mutated Breast Cancer. *Cancers* **2019**, *11*, 737. doi: 10.3390/cancers11060737.

25. Ayati, A.; Moghimi, S.; Salarinejad, S.; Safavi, M.; Pouramiri, B.; Foroumadi, A. A Review on Progression of Epidermal Growth Factor Receptor (EGFR) Inhibitors as an Efficient Approach in Cancer Targeted Therapy. *Bioorg. Chem.* **2020**, *99*, 103811. doi: 10.1016/j.bioorg.2020.103811.

26. Hurvitz, S.A.; Saura, C.; Oliveira, M.; Trudeau, M.E.; Moy, B.; Delaloge, S.; Gradishar, W.; Kim, S.-B.; Haley, B.; Ryvo, L., et al. Efficacy of Neratinib Plus Capecitabine in the Subgroup of Patients with Central Nervous System Involvement from the NALA Trial. *Oncologist* **2021**, *26*, e1327-e1338. doi: 10.1002/onco.13830.

27. Bachelot, T.; Romieu, G.; Campone, M.; Diéras, V.; Cropet, C.; Dalenc, F.; Jimenez, M.; Le Rhun, E.; Pierga, J.Y.; Gonçalves, A.; Leheurteur, M.; Domont, J.; Gutierrez, M.; Curé, H.; Ferrero, J.M.; Labbe-Devilliers, C. Lapatinib Plus Capecitabine in Patients with Previously Untreated Brain Metastases from HER2-Positive Metastatic Breast Cancer (LANDSCAPE): a Single-Group Phase 2 Study. *Lancet Oncol.* **2013**, *14*, 64-71. doi: 10.1016/S1470-2045(12)70432-1.

28. Scaltriti, M.; Rojo, F.; Ocaña, A.; Anido, J.; Guzman, M.; Cortes, J.; Di Cosimo, S.; Matias-Guiu, X.; Ramon y Cajal, S.; Arribas, J.; Baselga, J. Expression of p95HER2, a Truncated Form of the HER2 Receptor, and Response to Anti-HER2 Therapies in Breast Cancer. *J. Natl. Cancer Inst.* **2007**, *99*, 628-638. doi: 10.1093/jnci/djk134.

29. Conlon, N.T.; Kooijman, J.J.; van Gerwen, S.J.C.; Mulder, W.R.; Zaman, G.J.R.; Diala, I.; Eli, L.D.; Lalani, A.S.; Crown, J.; Collins, D.M. Comparative Analysis of Drug Response and Gene Profiling of HER2-Targeted Tyrosine Kinase Inhibitors. *Br. J. Cancer* **2021**, *124*, 1249-1259. doi: 10.1038/s41416-020-01257-x.

30. Kulukian, A.; Lee, P.; Taylor, J.; Rosler, R.; de Vries, P.; Watson, D.; Forero-Torres, A.; Peterson, S. Preclinical Activity of HER2-Selective Tyrosine Kinase Inhibitor Tucatinib as a Single Agent or in Combination with Trastuzumab or Docetaxel in Solid Tumor Models. *Mol. Cancer Ther.* **2020**, *19*, 976-987. doi: 10.1158/1535-7163.Mct-19-0873.

31. Singh, H.; Walker, A.J.; Amiri-Kordestani, L.; Cheng, J.; Tang, S.; Balcazar, P.; Barnett-Ringgold, K.; Palmby, T.R.; Cao, X.; Zheng, N., et al. U.S. Food and Drug Administration Approval: Neratinib for the Extended Adjuvant Treatment of Early-Stage HER2-Positive Breast Cancer. *Clin. Cancer Res.* **2018**, *24*, 3486-3491. doi: 10.1158/1078-0432.Ccr-17-3628.

32. U.S. Food and Drug Administration. FDA Approves Neratinib for Metastatic HER2-Positive Breast Cancer. *Approved Drug Products with Therapeutic Equivalence Evaluations (Orange Book) Short Description* [Online], 26 February 2020. https://www.fda.gov/drugs/resources-information-approved-drugs/fda-approves-neratinib-metastatic-her2-positive-breast-cancer (accessed 2023-02-26).

33. Berndt, N.; Karim, R.M.; Schönbrunn, E. Advances of Small Molecule Targeting of Kinases. *Curr. Opin. Chem. Biol.* **2017**, *39*, 126-132. doi: 10.1016/j.cbpa.2017.06.015.

34. Lu, X.; Yu, L.; Zhang, Z.; Ren, X.; Smaill, J.B.; Ding, K. Targeting EGFR$^{L858R/T790M}$ and EGFR$^{L858R/T790M/C7975}$ Resistance Mutations in NSCLC: Current Developments in Medicinal Chemistry. *Med. Res. Rev.* **2018**, *38*, 1550-1581. doi: 10.1002/med.21488.

35. Camidge, D.R.; Pao, W.; Sequist, L.V. Acquired Resistance to TKIs in Solid Tumours: Learning from Lung Cancer. *Nat. Rev. Clin. Oncol.* **2014**, *11*, 473-481. doi: 10.1038/nrclinonc.2014.104.

36. Yun, C.-H.; Boggon, T.J.; Li, Y.; Woo, M.S.; Greulich, H.; Meyerson, M.; Eck, M.J. Structures of Lung Cancer-Derived EGFR Mutants and Inhibitor Complexes: Mechanism of Activation and Insights into Differential Inhibitor Sensitivity. *Cancer Cell* **2007**, *11*, 217-227. doi: 10.1016/j.ccr.2006.12.017.

37. Singh, P.K.; Silakari, O. Chemotherapeutics-Resistance "Arms" Race: An Update on Mechanisms Involved in Resistance Limiting EGFR Inhibitors in Lung Cancer. *Life Sci.* **2017**, *186*, 25-32. doi: 10.1016/j.lfs.2017.08.001.

38. Yun, C.-H.; Mengwasser, K.E.; Toms, A.V.; Woo, M.S.; Greulich, H.; Wong, K.-K.; Meyerson, M.; Eck, M.J. The T790M Mutation in EGFR Kinase Causes Drug Resistance by Increasing the Affinity for ATP. *Proc. Natl. Acad. Sci.* **2008**, *105*, 2070. doi: 10.1073/pnas.0709662105.

39. Zhou, W.; Ercan, D.; Chen, L.; Yun, C.-H.; Li, D.; Capelletti, M.; Cortot, A.B.; Chirieac, L.; Iacob, R.E.; Padera, R.; Engen, J.R.; Wong, K.-K.; Eck, M.J.; Gray, N.S.; Jänne, P.A. Novel Mutant-Selective EGFR Kinase Inhibitors Against EGFR T790M. *Nature* **2009**, *462*, 1070-1074. doi: 10.1038/nature08622.

40. Pisa, R.; Kapoor, T.M. Chemical Strategies to Overcome Resistance Against Targeted Anticancer Therapeutics. *Nat. Chem. Biol.* **2020**, *16*, 817-825. doi: 10.1038/s41589-020-0596-8.

41. Singh, J. The Ascension of Targeted Covalent Inhibitors. *J. Med. Chem.* **2022**, *65*, 5886-5901. doi: 10.1021/acs.jmedchem.1c02134.

42. Paranjpe, R.; Basatneh, D.; Tao, G.; De Angelis, C.; Noormohammed, S.; Ekinci, E.; Abughosh, S.; Ghose, R.; Trivedi, M.V. Neratinib in HER2-Positive Breast Cancer Patients. *Ann. Pharmacother.* **2019**, *53*, 612-620. doi: 10.1177/1060028018824088.

43. Schlam, I.; Swain, S.M. HER2-Positive Breast Cancer and Tyrosine Kinase Inhibitors: The Time Is Now. *npj Breast Cancer* **2021**, *7*, 56. doi: 10.1038/s41523-021-00265-1.

44. Le Du, F.; Diéras, V.; Curigliano, G. The Role of Tyrosine Kinase Inhibitors in the Treatment of HER2+ Metastatic Breast Cancer. *Eur. J. Cancer* **2021**, *154*, 175-189. doi: 10.1016/j.ejca.2021.06.026.

45. Abdeldayem, A.; Raouf, Y.S.; Constantinescu, S.N.; Moriggl, R.; Gunning, P.T. Advances in Covalent Kinase Inhibitors. *Chem. Soc. Rev.* **2020**, *49*, 2617-2687. doi: 10.1039/C9CS00720B.

46. Ghosh, A.K.; Samanta, I.; Mondal, A.; Liu, W.R. Covalent Inhibition in Drug Discovery. *ChemMedChem* **2019**, *14*, 889-906. doi: 10.1002/cmdc.201900107.

47. Hossam, M.; Lasheen, D.S.; Abouzid, K.A.M. Covalent EGFR Inhibitors: Binding Mechanisms, Synthetic Approaches, and Clinical Profiles. *Arch. Pharm. Chem. Life Sci.* **2016**, *349*, 573-593. doi: 10.1002/ardp.201600063.

48. Abourehab, M.A.S.; Alqahtani, A.M.; Youssif, B.G.M.; Gouda, A.M. Globally Approved EGFR Inhibitors: Insights into Their Syntheses, Target Kinases, Biological Activities, Receptor Interactions, and Metabolism. *Molecules* **2021**, *26*, 6677. doi: 10.3390/molecules26216677.

49. Singh, M.; Jadhav, H.R. Targeting Non-Small Cell Lung Cancer with Small-Molecule EGFR Tyrosine Kinase Inhibitors. *Drug Discov. Today* **2018**, *23*, 745-753. doi: 10.1016/j.drudis.2017.10.004.

50. Nagasaka, M.; Zhu, V.W.; Lim, S.M.; Greco, M.; Wu, F.; Ou, S.-H.I. Beyond Osimertinib: The Development of Third-Generation EGFR Tyrosine Kinase Inhibitors For Advanced *EGFR+* NSCLC. *J. Thorac. Oncol.* **2021**, *16*, 740-763. doi: 10.1016/j.jtho.2020.11.028.

51. Liu, Q.; Sabnis, Y.; Zhao, Z.; Zhang, T.; Buhrlage, S.J.; Jones, L.H.; Gray, N.S. Developing Irreversible Inhibitors of the Protein Kinase Cysteinome. *Chem. Biol.* **2013**, *20*, 146-159. doi: 10.1016/j.chembiol.2012.12.006.

52. Singh, J.; Petter, R.C.; Baillie, T.A.; Whitty, A. The Resurgence of Covalent Drugs. *Nat. Rev. Drug Discov.* **2011**, *10*, 307-317. doi: 10.1038/nrd3410.

53. Barf, T.; Kaptein, A. Irreversible Protein Kinase Inhibitors: Balancing the Benefits and Risks. *J. Med. Chem.* **2012**, *55*, 6243-6262. doi: 10.1021/jm3003203.

54. Mons, E.; Jansen, I.D.C.; Loboda, J.; van Doodewaerd, B.R.; Hermans, J.; Verdoes, M.; van Boeckel, C.A.A.; van Veelen, P.A.; Turk, B.; Turk, D.; Ovaa, H. The Alkyne Moiety as a Latent Electrophile in Irreversible Covalent Small Molecule Inhibitors of Cathepsin K. *J. Am. Chem. Soc.* **2019**, *141*, 3507-3514. doi: 10.1021/jacs.8b11027.

55. Wissner, A.; Mansour, T.S. The Development of HKI-272 and Related Compounds for the Treatment of Cancer. *Arch. Pharm. Pharm. Med. Chem.* **2008**, *341*, 465-477. doi: 10.1002/ardp.200800009.

56. Tsou, H.-R.; Overbeek-Klumpers, E.G.; Hallett, W.A.; Reich, M.F.; Floyd, M.B.; Johnson, B.D.; Michalak, R.S.; Nilakantan, R.; Discafani, C.; Golas, J.; Rabindran, S.K.; Shen, R.; Shi, X.; Wang, Y.-F.; Upeslacis, J.; Wissner, A. Optimization of 6,7-Disubstituted-4-(arylamino)quinoline-3-carbonitriles as Orally Active, Irreversible Inhibitors of Human Epidermal Growth Factor Receptor-2 Kinase Activity. *J. Med. Chem.* **2005**, *48*, 1107-1131. doi: 10.1021/jm040159c.

57. Papamichelakis, M.; Chew, W. Method of Preparing 3-Cyano-quinolines and Intermediates Made Thereby. US20060270669A1, 30 November, 2006.

58. Wissner, A.; Rabindran Sridhar, K.; Tsou, H.-R. Protein Tyrosine Kinase Enzyme Inhibitors. US20050059678A1, 17 March, 2005.

59. Wissner, A.; Rabindran Sridhar, K.; Tsou, H.-R. Substituted Quinolines as Protein Tyrosine Kinase Enzyme Inhibitors. WO2005034955A1, 21 April, 2005.

60. Surry, D.S.; Buchwald, S.L. Dialkylbiaryl Phosphines in Pd-Catalyzed Amination: A User's Guide. *Chem. Sci.* **2011**, *2*, 27-50. doi: 10.1039/C0SC00331J.

61. Keeley, A.; Ábrányi-Balogh, P.; Keserű, G.M. Design and Characterization of a Heterocyclic Electrophilic Fragment Library for the Discovery of Cysteine-Targeted Covalent Inhibitors. *MedChemComm* **2019**, *10*, 263-267. doi: 10.1039/C8MD00327K.

62. Cee, V.J.; Volak, L.P.; Chen, Y.; Bartberger, M.D.; Tegley, C.; Arvedson, T.; McCarter, J.; Tasker, A.S.; Fotsch, C. Systematic Study of the Glutathione (GSH) Reactivity of N-Arylacrylamides: 1. Effects of Aryl Substitution. *J. Med. Chem.* **2015**, *58*, 9171-9178. doi: 10.1021/acs.jmedchem.5b01018.

63. Dahal, U.P.; Obach, R.S.; Gilbert, A.M. Benchmarking *In Vitro* Covalent Binding Burden As a Tool To Assess Potential Toxicity Caused by Nonspecific Covalent Binding of Covalent Drugs. *Chem. Res. Toxicol.* **2013**, *26*, 1739-1745. doi: 10.1021/tx400301q.

64. Flanagan, M.E.; Abramite, J.A.; Anderson, D.P.; Aulabaugh, A.; Dahal, U.P.; Gilbert, A.M.; Li, C.; Montgomery, J.; Oppenheimer, S.R.; Ryder, T., et al. Chemical and Computational Methods for the Characterization of Covalent Reactive Groups for the Prospective Design of Irreversible Inhibitors. *J. Med. Chem.* **2014**, *57*, 10072-10079. doi: 10.1021/jm501412a.

65. Ábrányi-Balogh, P.; Petri, L.; Imre, T.; Szijj, P.; Scarpino, A.; Hrast, M.; Mitrović, A.; Fonovič, U.P.; Németh, K.; Barreteau, H.; Roper, D.I.; Horváti, K.; Ferenczy, G.G.; Kos, J.; Ilaš, J.; Gobec, S.; Keserű, G.M. A Road Map for Prioritizing Warheads for Cysteine Targeting Covalent Inhibitors. *Eur. J. Med. Chem.* **2018**, *160*, 94-107. doi: 10.1016/j.ejmech.2018.10.010.

66. Lonsdale, R.; Burgess, J.; Colclough, N.; Davies, N.L.; Lenz, E.M.; Orton, A.L.; Ward, R.A. Expanding the Armory: Predicting and Tuning Covalent Warhead Reactivity. *J. Chem. Inf. Model.* **2017**, *57*, 3124-3137. doi: 10.1021/acs.jcim.7b00553.

67. Oballa, R.M.; Truchon, J.-F.; Bayly, C.I.; Chauret, N.; Day, S.; Crane, S.; Berthelette, C. A Generally Applicable Method for Assessing the Electrophilicity and Reactivity of Diverse Nitrile-Containing Compounds. *Bioorg. Med. Chem. Lett.* **2007**, *17*, 998-1002. doi: 10.1016/j.bmcl.2006.11.044.

68. Mons, E.; Kim, R.Q.; Mulder, M.P.C. Technologies for Direct Detection of Covalent Protein–Drug Adducts. *Pharmaceuticals* **2023**, *16*, 547. doi: 10.3390/ph16040547.

69. Gajiwala, K.S.; Feng, J.; Ferre, R.; Ryan, K.; Brodsky, O.; Weinrich, S.; Kath, J.C.; Stewart, A. Insights into the Aberrant Activity of Mutant EGFR Kinase Domain and Drug Recognition. *Structure* **2013**, *21*, 209-219. doi: 10.1016/j.str.2012.11.014.

70. Smith, S.; Keul, M.; Engel, J.; Basu, D.; Eppmann, S.; Rauh, D. Characterization of Covalent-Reversible EGFR Inhibitors. *ACS Omega* **2017**, *2*, 1563-1575. doi: 10.1021/acsomega.7b00157.

71. Donnelly, D.P.; Rawlins, C.M.; DeHart, C.J.; Fornelli, L.; Schachner, L.F.; Lin, Z.; Lippens, J.L.; Aluri, K.C.; Sarin, R.; Chen, B., et al. Best Practices and Benchmarks for Intact Protein Analysis for Top-Down Mass Spectrometry. *Nat. Meth.* **2019**, *16*, 587-594. doi: 10.1038/s41592-019-0457-0.

72. Zhang, Y.; Fonslow, B.R.; Shan, B.; Baek, M.-C.; Yates, J.R. Protein Analysis by Shotgun/Bottom-Up Proteomics. *Chem. Rev.* **2013**, *113*, 2343-2394. doi: 10.1021/cr3003533.

73. Jura, N.; Endres, N.F.; Engel, K.; Deindl, S.; Das, R.; Lamers, M.H.; Wemmer, D.E.; Zhang, X.; Kuriyan, J. Mechanism for Activation of the EGF Receptor Catalytic Domain by the Juxtamembrane Segment. *Cell* **2009**, *137*, 1293-1307. doi: 10.1016/j.cell.2009.04.025.

74. Cho, J.; Kim, S.; Du, J.; Meyerson, M. Autophosphorylation of the Carboxyl-Terminal Domain Is Not Required for Oncogenic Transformation by Lung-Cancer Derived EGFR Mutants. *Int. J. Cancer* **2018**, *143*, 679-685. doi: 10.1002/ijc.31332.

75. Gehringer, M. Covalent Inhibitors: Back On Track? *Future Med. Chem.* **2020**, *12*, 1363-1368. doi: 10.4155/fmc-2020-0118.

5

76. Harling, J.D.; Deakin, A.M.; Campos, S.; Grimley, R.; Chaudry, L.; Nye, C.; Polyakova, O.; Bessant, C.M.; Barton, N.; Somers, D.; Barrett, J.; Graves, R.H.; Hanns, L.; Kerr, W.J.; Solari, R. Discovery of Novel Irreversible Inhibitors of Interleukin (IL)-2-inducible Tyrosine Kinase (Itk) by Targeting Cysteine 442 in the ATP Pocket. *J. Biol. Chem.* **2013**, *288*, 28195-28206. doi: 10.1074/jbc.M113.474114.

77. Lebakken, C.S.; Riddle, S.M.; Singh, U.; Frazee, W.J.; Eliason, H.C.; Gao, Y.; Reichling, L.J.; Marks, B.D.; Vogel, K.W. Development and Applications of a Broad-Coverage, TR-FRET-Based Kinase Binding Assay Platform. *J. Biomol. Screen.* **2009**, *14*, 924-935. doi: 10.1177/1087057109339207.

78. *Optimization of a LanthaScreen™ Eu Kinase Binding Assay for EGFR*; Manual version 1; Invitrogen: pp 1-17. https://assets.thermofisher.com/TFS-Assets/LSG/manuals/EGFR_LanthaScreen_Binding.pdf (accessed 2021-07-23).

79. *HTRF A Guide To Homogeneous Time Resolved Fluorescence*; Cisbio Bioassays: 2018. https://www.bio-connectdiagnostics.nl/uploads/pdf/Cisbio-A_Guide_to_HTRF_2693.pdf (accessed 2021-07-23).

80. Crawford, K. *Developing a Time-Resolved Fluorescence Resonance Energy Transfer (TR-FRET) Assay*; AppNote 3./01; Molecular Devices: 2001. http://mdc.custhelp.com/euf/assets/content/Analyst_App_Note_TR-FRET%20App%20note.pdf (accessed 2021-07-23).

81. Schiele, F.; Ayaz, P.; Fernández-Montalván, A. A Universal Homogeneous Assay for High-Throughput Determination of Binding Kinetics. *Anal. Biochem.* **2015**, *468*, 42-49. doi: 10.1016/j.ab.2014.09.007.

82. Georgi, V.; Schiele, F.; Berger, B.-T.; Steffen, A.; Marin Zapata, P.A.; Briem, H.; Menz, S.; Preusse, C.; Vasta, J.D.; Robers, M.B.; Brands, M.; Knapp, S.; Fernández-Montalván, A. Binding Kinetics Survey of the Drugged Kinome. *J. Am. Chem. Soc.* **2018**, *140*, 15774-15782. doi: 10.1021/jacs.8b08048.

83. Davis, M.I.; Hunt, J.P.; Herrgard, S.; Ciceri, P.; Wodicka, L.M.; Pallares, G.; Hocker, M.; Treiber, D.K.; Zarrinkar, P.P. Comprehensive Analysis of Kinase Inhibitor Selectivity. *Nat. Biotechnol.* **2011**, *29*, 1046-1051. doi: 10.1038/nbt.1990.

84. Lategahn, J.; Keul, M.; Klövekorn, P.; Tumbrink, H.L.; Niggenaber, J.; Müller, M.P.; Hodson, L.; Flaßhoff, M.; Hardick, J.; Grabe, T., et al. Inhibition of Osimertinib-Resistant Epidermal Growth Gactor Receptor EGFR-T790M/C797S. *Chem. Sci.* **2019**, *10*, 10789-10801. doi: 10.1039/C9SC03445E.

85. Wang, Y.; Ma, H. Protein Kinase Profiling Assays: A Technology Review. *Drug Discov. Today: Technol.* **2015**, *18*, 1-8. doi: 10.1016/j.ddtec.2015.10.007.

86. González-Vera, J.A. Probing the Kinome in Real Time with Fluorescent Peptides. *Chem. Soc. Rev.* **2012**, *41*, 1652-1664. doi: 10.1039/C1CS15198C.

87. Tardieu, J.-L. HTRF® KinEASE™ TK: A New Solution for Tyrosine Kinase Screening. *Nat. Meth.* **2007**, *4*, i-ii. doi: 10.1038/nmeth1082.

88. Zegzouti, H.; Zdanovskaia, M.; Hsiao, K.; Goueli, S.A. ADP-Glo: A Bioluminescent and Homogeneous ADP Monitoring Assay for Kinases. *Assay Drug Dev. Technol.* **2009**, *7*, 560-572. doi: 10.1089/adt.2009.0222.

89. Wang, Z.; Candelora, C. In Vitro Enzyme Kinetics Analysis of EGFR. *Methods Mol. Biol.* **2017**, *1487*, 23-33. doi: 10.1007/978-1-4939-6424-6_2.

90. Shults, M.D.; Janes, K.A.; Lauffenburger, D.A.; Imperiali, B. A Multiplexed Homogeneous Fluorescence-Based assay for Protein Kinase Activity in Cell Lysates. *Nat. Meth.* **2005**, *2*, 277-284. doi: 10.1038/nmeth747.

91. Luković, E.; González-Vera, J.A.; Imperiali, B. Recognition-Domain Focused Chemosensors: Versatile and Efficient Reporters of Protein Kinase Activity. *J. Am. Chem. Soc.* **2008**, *130*, 12821-12827. doi: 10.1021/ja8046188.

92. Sjin, R.T.T.; Lee, K.; Walter, A.O.; Dubrovskiy, A.; Sheets, M.; St Martin, T.; Labenski, M.T.; Zhu, Z.; Tester, R.; Karp, R., et al. *In Vitro* and *In Vivo* Characterization of Irreversible Mutant-Selective EGFR Inhibitors That Are Wild-Type Sparing. *Mol. Cancer Ther.* **2014**, *13*, 1468-1479. doi: 10.1158/1535-7163.MCT-13-0966.

93. Schwartz, P.A.; Kuzmic, P.; Solowiej, J.; Bergqvist, S.; Bolanos, B.; Almaden, C.; Nagata, A.; Ryan, K.; Feng, J.; Dalvie, D.; Kath, J.C.; Xu, M.; Wani, R.; Murray, B.W. Covalent EGFR Inhibitor Analysis Reveals Importance of Reversible Interactions to Potency and Mechanisms of Drug Resistance. *Proc. Natl. Acad. Sci.* **2014**, *111*, 173. doi: 10.1073/pnas.1313733111.

94. Cheng, H.; Nair, S.K.; Murray, B.W.; Almaden, C.; Bailey, S.; Baxi, S.; Behenna, D.; Cho-Schultz, S.; Dalvie, D.; Dinh, D.M., et al. Discovery of 1-{(3R,4R)-3-[({5-Chloro-2-[(1-methyl-1H-pyrazol-4-yl)amino]-7H-pyrrolo[2,3-d]pyrimidin-4-yl}oxy)methyl]-4-methoxypyrrolidin-1-yl}prop-2-en-1-one (PF-06459988), a Potent, WT Sparing, Irreversible Inhibitor of T790M-Containing EGFR Mutants. *J. Med. Chem.* **2016**, *59*, 2005-2024. doi: 10.1021/acs.jmedchem.5b01633.

95. Planken, S.; Behenna, D.C.; Nair, S.K.; Johnson, T.O.; Nagata, A.; Almaden, C.; Bailey, S.; Ballard, T.E.; Bernier, L.; Cheng, H., et al. Discovery of N-((3R,4R)-4-Fluoro-1-(6-((3-methoxy-1-methyl-1H-pyrazol-4-yl)amino)-9-methyl-9H-purin-2-yl)pyrrolidine-3-yl)acrylamide (PF-06747775) through Structure-Based Drug Design: A High Affinity Irreversible Inhibitor Targeting Oncogenic EGFR Mutants with Selectivity over Wild-Type EGFR. *J. Med. Chem.* **2017**, *60*, 3002-3019. doi: 10.1021/acs.jmedchem.6b01894.

96. Zhai, X.; Ward, R.A.; Doig, P.; Argyrou, A. Insight into the Therapeutic Selectivity of the Irreversible EGFR Tyrosine Kinase Inhibitor Osimertinib through Enzyme Kinetic Studies. *Biochemistry* **2020**, *59*, 1428-1441. doi: 10.1021/acs.biochem.0c00104.

97. Walter, A.O.; Sjin, R.T.T.; Haringsma, H.J.; Ohashi, K.; Sun, J.; Lee, K.; Dubrovskiy, A.; Labenski, M.; Zhu, Z.; Wang, Z., et al. Discovery of a Mutant-Selective Covalent Inhibitor of EGFR that Overcomes T790M-Mediated Resistance in NSCLC. *Cancer Discov.* **2013**, *3*, 1404-1415. doi: 10.1158/2159-8290.CD-13-0314.

98. Laufer, S.; Bajorath, J.; Gehringer, M.; Gray, N.; Frye, S.; Lindsley, C.W. Publication Criteria and Requirements for Studies on Protein Kinase Inhibitors—What Is Expected? *J. Med. Chem.* **2022**, *65*, 6973-6974. doi: 10.1021/acs.jmedchem.2c00623.

99. Mons, E.; Roet, S.; Kim, R.Q.; Mulder, M.P.C. A Comprehensive Guide for Assessing Covalent Inhibition in Enzymatic Assays Illustrated with Kinetic Simulations. *Curr. Protoc.* **2022**, *2*, e419. doi: 10.1002/cpz1.419.

100. Hoyt, K.W.; Urul, D.A.; Ogboo, B.C.; Wittlinger, F.; Laufer, S.A.; Schaefer, E.M.; May, E.W.; Heppner, D.E. Pitfalls and Considerations in Determining the Potency and Mutant Selectivity of Covalent Epidermal Growth Factor Receptor Inhibitors. *ChemRxiv* **2023**. doi: 10.26434/chemrxiv-2023-tkqqk.

101. *PhosphoSens® Protein Kinase Assay Instruction Manual*; #1001.007; AssayQuant Technologies: 2020. https://www.assayquant.com/resources.

102. Guan, I.; Williams, K.; Pan, J.; Liu, X. New Cysteine Covalent Modification Strategies Enable Advancement of Proteome-wide Selectivity of Kinase Modulators. *Asian J. Org. Chem.* **2021**, *10*, 949-963. doi: 10.1002/ajoc.202100036.

103. Sapmaz, A.; Berlin, I.; Bos, E.; Wijdeven, R.H.; Janssen, H.; Konietzny, R.; Akkermans, J.J.; Erson-Bensan, A.E.; Koning, R.I.; Kessler, B.M.; Neefjes, J.; Ovaa, H. USP32 Regulates Late Endosomal Transport and Recycling Through Deubiquitylation of Rab7. *Nat. Commun.* **2019**, *10*, 1454. doi: 10.1038/s41467-019-09437-x.

104. Cicek, E.; Circir, A.; Oyken, M.; Akbulut Caliskan, O.; Dioken, D.N.; Guntekin Ergun, S.; Cetin-Atalay, R.; Sapmaz, A.; Ovaa, H.; Sahin, O.; Erson-Bensan, A.E. EGF-SNX3-EGFR Axis Drives Tumor Progression and Metastasis in Triple-Negative Breast Cancers. *Oncogene* **2022**, *41*, 220-232. doi: 10.1038/s41388-021-02086-9.

105. EGFR. In *The Human Protein Atlas* [Online]. https://www.proteinatlas.org/ENSG00000146648-EGFR/cell+line

106. ERBB2. In *The Human Protein Atlas* [Online]. https://www.proteinatlas.org/ENSG00000141736-ERBB2/cell+line

107. Chen, B.; Mao, R.; Wang, H.; She, J.-X. Cell Line and Drug-Dependent Effect of ERBB3 on Cancer Cell Proliferation, Chemosensitivity, and Multidrug Actions. *Int. J. High Throughput Screen.* **2010**, *1*, 49-55. doi: 10.2147/IJHTS.S8235.

108. Brescia, P.J.; Banks, P.; Cornell-Kennon, S.; Schaefer, E.; Imperiali, B. *Monitoring of Protein Kinase Activity Using Next Generation CSox-based Substrate Sensors*; AppNote #AN080117_07; BioTek Instruments: 2017. https://www.biotek.com/resources/application-notes/monitoring-of-protein-kinase-activity-using-next-generation-csox-based-substrate-sensors/ (accessed 2021-07-26).

109. Shults, M.D.; Imperiali, B. Versatile Fluorescence Probes of Protein Kinase Activity. *J. Am. Chem. Soc.* **2003**, *125*, 14248-14249. doi: 10.1021/ja0380502.

110. Carey, K.D.; Garton, A.J.; Romero, M.S.; Kahler, J.; Thomson, S.; Ross, S.; Park, F.; Haley, J.D.; Gibson, N.; Sliwkowski, M.X. Kinetic Analysis of Epidermal Growth Factor Receptor Somatic Mutant Proteins Shows Increased Sensitivity to the Epidermal Growth Factor Receptor Tyrosine Kinase Inhibitor, Erlotinib. *Cancer Res.* **2006**, *66*, 8163-8171. doi: 10.1158/0008-5472.Can-06-0453.

111. Baulida, J.; Kraus, M.H.; Alimandi, M.; Fiore, P.P.D.; Carpenter, G. All ErbB Receptors Other Than the Epidermal Growth Factor Receptor Are Endocytosis Impaired. *J. Biol. Chem.* **1996**, *271*, 5251-5257. doi: 10.1074/jbc.271.9.5251.

112. Rabindran, S.K.; Discafani, C.M.; Rosfjord, E.C.; Baxter, M.; Floyd, M.B.; Golas, J.; Hallett, W.A.; Johnson, B.D.; Nilakantan, R.; Overbeek, E.; Reich, M.F.; Shen, R.; Shi, X.; Tsou, H.-R.; Wang, Y.-F.; Wissner, A. Antitumor Activity of HKI-272, an Orally Active, Irreversible Inhibitor of the HER-2 Tyrosine Kinase. *Cancer Res.* **2004**, *64*, 3958-3965. doi: 10.1158/0008-5472.CAN-03-2868.

113. Awoonor-Williams, E.; Rowley, C.N. How Reactive are Druggable Cysteines in Protein Kinases? *J. Chem. Inf. Model.* **2018**, *58*, 1935-1946. doi: 10.1021/acs.jcim.8b00454.

114. Lalmanach, G.; Saidi, A.; Bigot, P.; Chazeirat, T.; Lecaille, F.; Wartenberg, M. Regulation of the Proteolytic Activity of Cysteine Cathepsins by Oxidants. *Int. J. Mol. Sci.* **2020**, *21*, 1944. doi: 10.3390/ijms21061944.

115. Harris, T.K.; Turner, G.J. Structural Basis of Perturbed pKa Values of Catalytic Groups in Enzyme Active Sites. *IUBMB Life* **2002**, *53*, 85-98. doi: 10.1080/15216540211468.

116. Discafani, C.M.; Carroll, M.L.; Floyd, M.B.; Hollander, I.J.; Husain, Z.; Johnson, B.D.; Kitchen, D.; May, M.K.; Malo, M.S.; Minnick, A.A.; Nilakantan, R.; Shen, R.; Wang, Y.-F.; Wissner, A.; Greenberger, L.M. Irreversible Inhibition of Epidermal Growth Factor Receptor Tyrosine Kinase with *In Vivo* Activity by *N*-[4-[(3-bromophenyl)amino]-6-quinazolinyl]-2-butynamide (CL-387,785). *Biochem. Pharmacol.* **1999**, *57*, 917-925. doi: 10.1016/S0006-2952(98)00356-6.

117. Wood, E.R.; Shewchuk, L.M.; Ellis, B.; Brignola, P.; Brashear, R.L.; Caferro, T.R.; Dickerson, S.H.; Dickson, H.D.; Donaldson, K.H.; Gaul, M., et al. 6-Ethynylthieno[3,2-d]- and 6-Ethynylthieno[2,3-d]pyrimidin-4-anilines as Tunable Covalent Modifiers of ErbB Kinases. *Proc. Natl. Acad. Sci.* **2008**, *105*, 2773. doi: 10.1073/pnas.0708281105.

118. Boschelli, D.H.; Wang, D.Y.; Ye, F.; Yamashita, A.; Zhang, N.; Powell, D.; Weber, J.; Boschelli, F. Inhibition of Src Kinase Activity by 4-anilino-7-thienyl-3-quinolinecarbonitriles. *Bioorg. Med. Chem. Lett.* **2002**, *12*, 2011-2014. doi: 10.1016/S0960-894X(02)00302-5.

119. Boschelli, D.H.; Wang, Y.D.; Ye, F.; Wu, B.; Zhang, N.; Dutia, M.; Powell, D.W.; Wissner, A.; Arndt, K.; Weber, J.M.; Boschelli, F. Synthesis and Src Kinase Inhibitory Activity of a Series of 4-Phenylamino-3-quinolinecarbonitriles. *J. Med. Chem.* **2001**, *44*, 822-833. doi: 10.1021/jm000420z.

120. Chen, D.; Guo, D.; Yan, Z.; Zhao, Y. Allenamide As a Bioisostere of Acrylamide in the Design and Synthesis of Targeted Covalent Inhibitors. *MedChemComm* **2018**, *9*, 244-253. doi: 10.1039/C7MD00571G.

121. Klutchko, S.R.; Zhou, H.; Winters, R.T.; Tran, T.P.; Bridges, A.J.; Althaus, I.W.; Amato, D.M.; Elliott, W.L.; Ellis, P.A.; Meade, M.A., et al. Tyrosine Kinase Inhibitors. 19. 6-Alkynamides of 4-Anilinoquinazolines and 4-Anilinopyrido[3,4-d]pyrimidines as Irreversible Inhibitors of the erbB Family of Tyrosine Kinase Receptors. *J. Med. Chem.* **2006**, *49*, 1475-1485. doi: 10.1021/jm050936o.

122. Luna-Vargas, M.P.A.; Christodoulou, E.; Alfieri, A.; van Dijk, W.J.; Stadnik, M.; Hibbert, R.G.; Sahtoe, D.D.; Clerici, M.; Marco, V.D.; Littler, D.; Celie, P.H.N.; Sixma, T.K.; Perrakis, A. Enabling High-Throughput Ligation-independent Cloning and Protein Expression for the Family of Ubiquitin Specific Proteases. *J. Struct. Biol.* **2011**, *175*, 113-119. doi: 10.1016/j.jsb.2011.03.017.

123. Abramoff, M.; Magalhães, P.; Ram, S.J. Image Processing with ImageJ. *Biophotonics Intern.* **2003**, *11*, 36-42.

124. Rasband, W.S. *ImageJ*, U. S. National Institutes of Health, Bethesda, Maryland, USA: 1997-2018. https://imagej.nih.gov/ij/.

125. Schneider, C.A.; Rasband, W.S.; Eliceiri, K.W. NIH Image to ImageJ: 25 Years of Image Analysis. *Nat. Meth.* **2012**, *9*, 671-675. doi: 10.1038/nmeth.2089.

126. Carmi, C.; Galvani, E.; Vacondio, F.; Rivara, S.; Lodola, A.; Russo, S.; Aiello, S.; Bordi, F.; Costantino, G.; Cavazzoni, A.; Alfieri, R.R.; Ardizzoni, A.; Petronini, P.G.; Mor, M. Irreversible Inhibition of Epidermal Growth Factor Receptor Activity by 3-Aminopropanamides. *J. Med. Chem.* **2012**, *55*, 2251-2264. doi: 10.1021/jm201507x.

127. Blum, D.M.; Boschelli, D.H.; Feigelson, G.B.; Strong, H.L.; Wiggins Sutherland, K. Process for Preparation of 4-Amino-3-Quinolinecarbonitriles. US20050043537A1, 24 February, 2005.

128. Boschelli, D.H.; Wu, B.; Ye, F.; Wang, Y.; Golas, J.M.; Lucas, J.; Boschelli, F. Synthesis and Src Kinase Inhibitory Activity of a Series of 4-[(2,4-Dichloro-5-methoxyphenyl)amino]-7-furyl-3-quinolinecarbonitriles. *J. Med. Chem.* **2006**, *49*, 7868-7876. doi: 10.1021/jm061031t.

129. Fors, B.P.; Watson, D.A.; Biscoe, M.R.; Buchwald, S.L. A Highly Active Catalyst for Pd-Catalyzed Amination Reactions: Cross-Coupling Reactions Using Aryl Mesylates and the Highly Selective Monoarylation of Primary Amines Using Aryl Chlorides. *J. Am. Chem. Soc.* **2008**, *130*, 13552-13554. doi: 10.1021/ja8055358.

130. Kuzmič, P. *Biochemical/Biophysical Kinetics "Made Easy": Software DYNAFIT in Drug Discovery Research*; BioKin Ltd. http://www.biokin.com/slides/1212-novartis.pdf (accessed 2021-07-23).

131. *LanthaScreen® TR-FRET ER Beta Competitive Binding Assay*; MAN0010002; Life Technologies: 2014. http://tools.thermofisher.com/content/sfs/manuals/lanthascreen_tr_fret_er_beta_comp_binding_assay_man.pdf (accessed 2021-07-23).

132. Ulusu, N.N. Evolution of Enzyme Kinetic Mechanisms. *J. Mol. Evol.* **2015**, *80*, 251-257. doi: 10.1007/s00239-015-9681-0.

133. Posner, I.; Engel, M.; Levitzki, A. Kinetic Model of the Epidermal Growth Factor (EGF) Receptor Tyrosine Kinase and a Possible Mechanism of Its Activation by EGF. *J. Biol. Chem.* **1992**, *267*, 20638-20647. doi: 10.1016/S0021-9258(19)36734-1.

134. Reytor González, M.L.; Cornell-Kennon, S.; Schaefer, E.; Kuzmič, P. An Algebraic Model to Determine Substrate Kinetic Parameters by Global Nonlinear Fit of Progress Curves. *Anal. Biochem.* **2017**, *518*, 16-24. doi: 10.1016/j.ab.2016.11.001.

135. Kuzmič, P. *Covalent Inhibition Kinetics: Application to EGFR Kinase*; BioKin Ltd: 2014. http://www.biokin.com/slides/1409-az.pdf (accessed 2021-07-23).

136. Adams, J. A. Kinetic and Catalytic Mechanisms of Protein Kinases. *Chem. Rev.* **2001**, *101*, 2271-2290. doi: 10.1021/cr000230w.

137. Kuzmič, P.; Solowiej, J.; Murray, B.W. An Algebraic Model for the Kinetics of Covalent Enzyme Inhibition at Low Substrate Concentrations. *Anal. Biochem.* **2015**, *484*, 82-90. doi: 10.1016/j.ab.2014.11.014.

138. Beck, J.R.; Peterson, L.B.; Imperiali, B.; Stains, C.I. Quantification of Protein Kinase Enzymatic Activity in Unfractionated Cell Lysates Using CSox-Based Sensors. *Curr. Protoc. Chem. Biol.* **2014**, *6*, 135-156. doi: 10.1002/9780470559277.ch140106.

5

7.   Supporting Information

7.1.   Literature Values for EGFR Activity and Inhibition
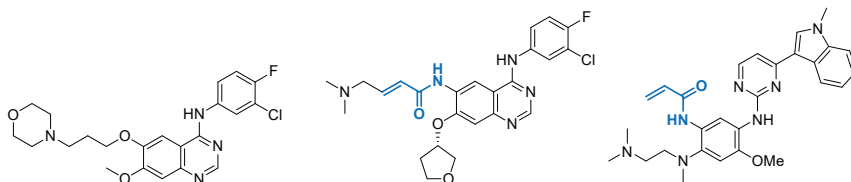
Biochemical IC$_{50}$ (nM)	gefitinib	afatinib	osimertinib
EGFR^{WT}	0.2	<0.1	1.0
EGFR^{L858R}	<0.1	<0.1	0.7
EGFR$^{L858R/T790M}$	185	0.3	0.3
EGFR$^{L858R/T790M/C797S}$	250	25	116

Figure S1 | Chemical structure, name, and *in vitro* biochemical IC$_{50}$ (nM) against recombinant EGFR (mutant) activity reported by Lategahn *et al*.[84] Covalent warheads are marked in blue.

Table S1 | Reported ATP affinity of (mutant) EGFR.[38]

	$K_{M,ATP}$ (µM)	k_{cat} (s^{-1})	$k_{cat}/K_{M,ATP}$ (×10^3 M^{-1}s^{-1})
EGFR^{WT}	5.2 ± 0.2	0.026	5
EGFR^{T790M}	5.9 ± 0.1	0.137	23
EGFR^{L858R}	148 ± 4	1.484	10
EGFR$^{L858R/T790M}$	8.4 ± 0.3	0.456	54

Table S2 | Reported biochemical IC$_{50}$ values (nM).

	erlotinib	gefitinib	lapatinib	neratinib	afatinib	vandetanib	staurosporine
EGFR^{WT}	0.67	1	2.4	1.1*	0.25*	9.5	370
EGFR^{T790M}	140	40	860	1.5*	0.61*	100	0.77
EGFR^{L858R}	0.97	0.94	2.8	0.67*	0.2*	8.7	270
EGFR$^{L858R/T790M}$	190	140	>10^4	27*	1.1*	230	0.35
HER2	2900	3500	7	6*	5*	2600	190
HER3	1100	790	5500	7.7*	4500*	160	>10^4
HER4	230	410	54	2.4*	6.3*	480	770
SRC	700	3800	>10^4	4100*	2800*	70	86

Inhibitor potency in ATP site-dependent competition binding assay (KINOMEscan Technology Platform).[83] * Values not corrected for irreversible covalent binding mode.

7.2. Chemical Synthesis

Precursor 6-bromoquinoline **2** was prepared at Mercachem (now: Symeres Nijmegen) (**Scheme S1**) by adaptation of reported methodology for large scale preparation of 4-amino-3-quinolinecarbonitriles targeting Src kinase domain [127-128] and 3-cyano-quinolines targeting the HER kinase family. [57]

Alkyne derivatives **8RK57** and **8RK58** were obtained in a single step from bromoquinoline **2** by Pd-catalyzed C–N cross-coupling with primary amines under Buchwald-Hartwig amination conditions. [60] BrettPhos Palladacycle G3 (L = BrettPhos) and BrettPhos are recommended Pd-(pre)catalyst and dialkylbiaryl phosphine ligand for mono *N*-arylation of primary aliphatic amines. [60] C-N cross-coupling with a secondary amine is much slower than with a primary amine, thus minimizing formation of undesired biarylation product or homocoupling product. [129]

5
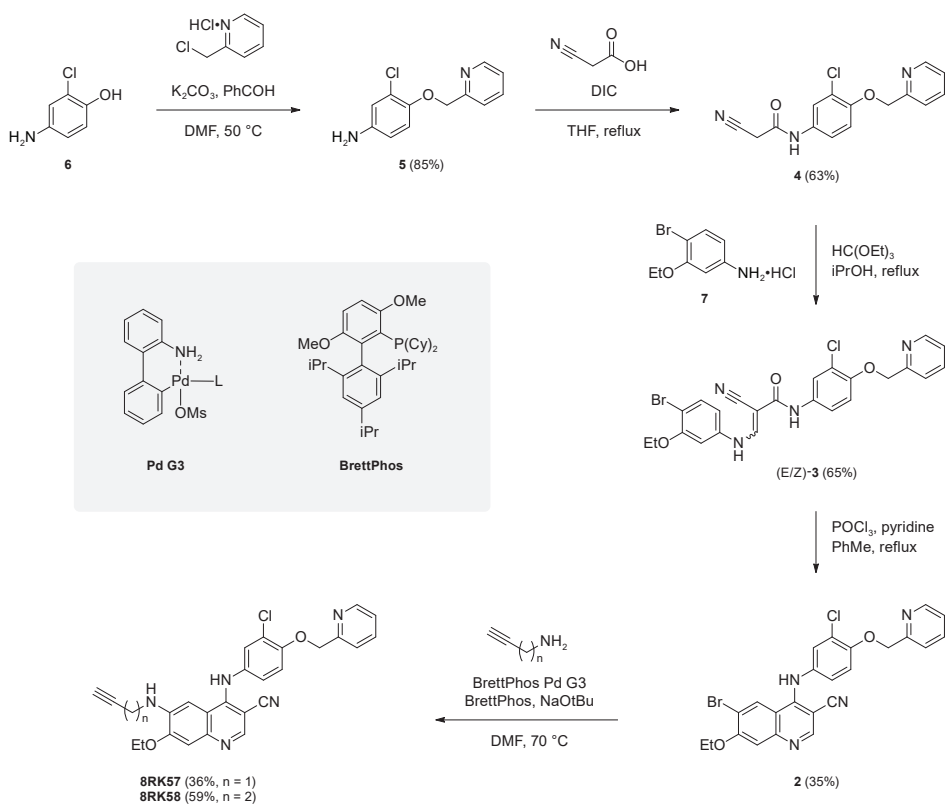
Scheme S1 | Chemical synthesis of neratinib derivatives. Alkylation of aminophenol **6** to form aniline **5** was followed by DIC-mediated amide coupling with cyanoacetic acid to afford acetamide **4**. Treatment of acetamide **4** with triethyl orthoformate and primary aniline **7** afforded cyanoacrylamide 3 as a mixture of the (E)- and (Z)-isomer. Subsequent phosphorus oxychloride-mediated ring closure resulted in the formation of 6-bromo-4-anilino-3-quinolinecarbonitrile **2**. Treatment of bromoquinoline **2** with excess propargylamine or 1-amino-3-butyne in presence of third generation Pd-precatalyst BrettPhos Palladacycle G3 and dialkylbiaryl phosphine ligand BrettPhos afforded alkyne derivatives **8RK57** and **8RK58**.

7.3. Thiol Reactivity Assay

Table S3 | Thiol Adduct Formation related to **Figure 3.**

Compound		Rt (min)	m/z (Da)	UV area at t (h)						GSH occupancy (%)
				0	1	2	3	4	24	
neratinib	Unbound	1.54	557.2	9859 / 9047	8138 / 7542	6567 / 5669	5576 / 5444	4599 / 4058	757 / 466	
	GSH Adduct	1.47	864.3	0 / 4.7	2246 / 2159	3380 / 3187	4105 / 3968	4397 / 4118	9019 / 8373	
	GSH occupancy (%)			0.05 ± 0.07	22 ± 0.49	35 ± 1.4	42 ± 0.14	50 ± 1.1	94 ± 1.7	
8RK57	Unbound	1.76	484.1	4237 / 3738	4103 / 3883	4197 / 4655	3992 / 4638	4165 / 4192	3987 / 4528	
	GSH Adduct	–	791.2	BLD / BLD	BLD / BLD	BLD / BLD	BLD / BLD	BLD / BLD	BLD / BLD	
	GSH occupancy (%)			0	0	0	0	0	0	
8RK58	Unbound	1.82	498.1	2666 / 2335	2380 / 1781	1762 / 1405	1822 / 1506	1194 / 1957	1106 / 1250	
	GSH Adduct	–	805.2	BLD / BLD	BLD / BLD	BLD / BLD	BLD / BLD	BLD / BLD	BLD / BLD	
	GSH occupancy (%)			0	0	0	0	0	0	
gefitinib	Unbound	1.50	447.1	15757 / 15363	17274 / 16853	17643 / 16490	16885 / 16356	17220 / 15568	16350 / 12481	
	GSH Adduct	–	754.2	BLD / BLD	BLD / BLD	BLD / BLD	BLD / BLD	BLD / BLD	BLD / BLD	
	GSH occupancy (%)			0	0	0	0	0	0	
afatinib	Unbound	1.51	486.1	7209 / 7331	4490 / 4530	2491 / 2601	1494 / 1492	897 / 860	41 / 38	
	GSH Adduct	1.45	793.2	40 / 49	3400 / 3642	4945 / 5274	6020 / 6175	6421 / 6617	6965 / 7137	
	GSH occupancy (%)			0.65 ± 0.07	44 ± 1.1	67 ± 0.35	80 ± 0.28	88 ± 0.57	99 ± 0.07	

LC-MS analysis of inhibitor (100 µM) incubated with 5 mM GSH in PBS pH7.5 at 37 °C. Quantification of unbound inhibitor and GSH adduct (+307 Da) from integration of UV absorbance area (λ_{abs} = 350 nm) following established protocol.[54, 67] BLD = below limit of detection. *Italic*: theoretical value for adduct (not observed). Details on calculations of GSH occupancy and kinetic fits can be found in *section 4.1*. Values for GSH occupancy are mean ± SD.
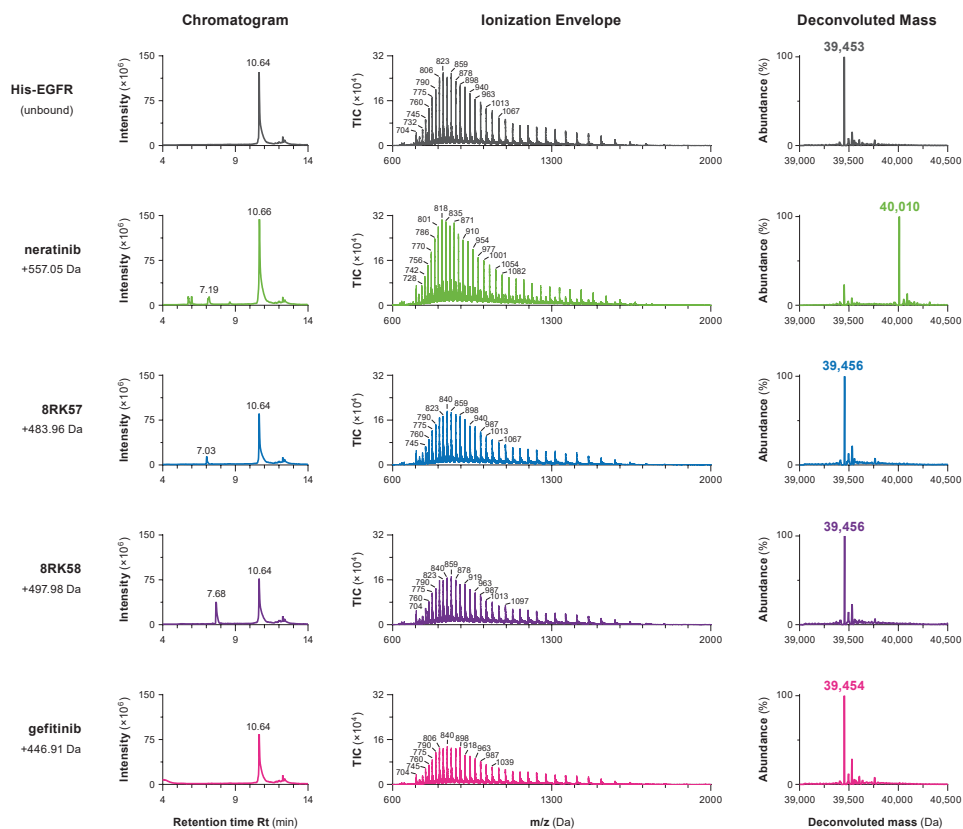
7.4. Intact Protein MS Analysis

Figure S2 | LC-MS traces for intact protein MS analysis of unbound His-EGFR (1 µM) incubated with inhibitor (100 µM) for 4 h at 21 °C. Data accompanying **Figure 4**. *Left:* UPLC chromatogram. *Middle:* Electrospray ionization mass spectrum. *Right:* Deconvoluted mass (average isotopes).

Table S4 | Screening conditions for covalent adduct formation (intact protein MS analysis).

compound	[compound]	Covalent adduct	
		4 h	24 h
DMSO	–	–	–
neratinib	100 µM	+[a]	+[b]
	10 µM	N.A.	+
8RK57	100 µM	–	–
	10 µM	N.A.	–
8RK58	100 µM	–	–
	10 µM	N.A.	–
gefitinib	100 µM	–	N.A.

Detection of covalent adduct by intact protein MS analysis. His-EGFR (1 µM) treated with excess compound is incubated at 21 °C for the indicated time. N.A. = not applicable. [a] 10:2 adduct/unbound EGFR. [b] 10:1:1 adduct/unbound/double adduct (double addition of compound).

5

7.5. Lanthascreen Kinase Binding Assay

Assay conditions were optimized to maximize the assay window while avoiding inhibitor depletion. An intrinsic issue with kinase binding assays is the minimum required kinase concentration for a detectable signal. We found that 2 nM GST-EGFR was the minimum kinase concentration. At lower kinase concentration, the signal at 620 nm originating from the FRET donor was too high, even in presence of GST-EGFR and FRET acceptor, because a large portion of EuAb is unbound ($K_{D,EuAb}$ = 0.6 nM).[130]

FRET acceptor kinase tracer 199 (KT199) was initially used at the recommended concentration of 25 nM.[78] The optimal tracer concentration depends on the tracer potency, desired competition and assay window. Tracer concentrations above 100 nM are not recommended as these could cause artefacts related to diffusion-enhanced TR-FRET: a signal that is not related to a biological binding event but the result of the FRET donor being in close proximity of the FRET acceptor in solution. Diffusion-enhanced FRET increases with a higher tracer concentration, thereby increasing the background (**Figure S3B**).[131] Tracer potency and assay window are linked properties: more kinase is engaged in the kinase-tracer complex at a high tracer concentration ([tracer] >> K_D), but if the tracer concentration is too high it induces diffusion-enhanced TR-FRET thus narrowing the assay window (**Figure S3C**).

Confronted with tight-binding behavior, tracer was increased to the maximum recommended concentration: competitive tracer binding would decrease the apparent inhibitor binding potency. Unfortunately, neratinib was unable to fully displace 100 nM tracer, and the resulting assay window was unsuitable to assess inhibitor binding potency (**Figure S3C**, *left*). Incomplete tracer dissociation may be caused by a secondary low-affinity tracer binding site or binding configuration uncompetitive with neratinib binding, thus interfering with tracer displacement at high tracer concentrations.
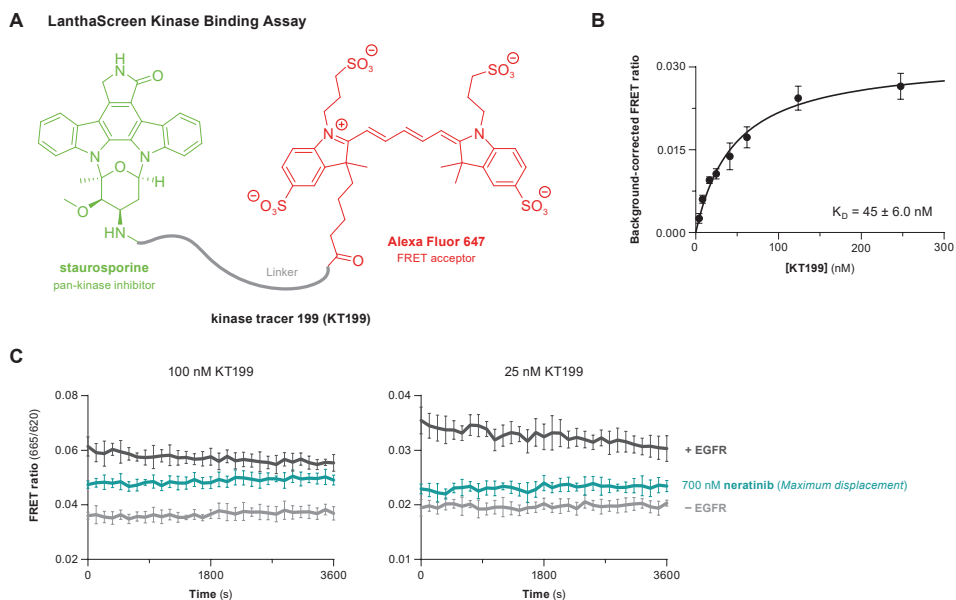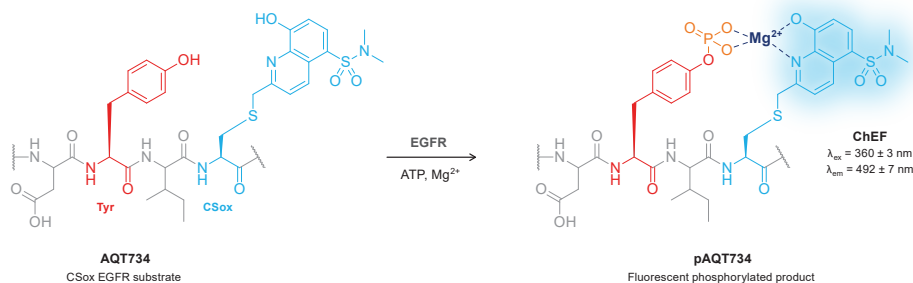

Figure S3 | *In vitro* Lanthascreen kinase binding assay. Data accompanying **Figure 5**. **(A)** KT199 is a conjugate of pan-kinase inhibitor staurosporine and FRET acceptor Alexa Fluor 647. **(B)** Calculation of tracer dissociation constant K_D after baseline correction: subtraction of EuAb + KT199 signal in absence of GST-EGFR. **(C)** Progress curves for 2 nM GST-EGFR with 100 nM KT199 *(left)* or 25 nM KT199 *(right)*. Maximum KT199 displacement by 700 nM neratinib is ineffective.

7.6.   PhosphoSens Kinase Activity Assay

EGFR-mediated substrate phosphorylation is a bisubstrate reaction which complicates algebraic evaluation of inhibition.[132-133] Fortunately, the reaction can be simplified to a (truncated) hit-and-run model $(E + S \rightarrow E + P)$ because a high ATP concentration (estimated $K_{M,ATP} \ll 1$ mM) and low CSox substrate concentration (estimated $K_{M,CSox} \gg 10$ µM) are used.[93, 134-136] Please consult the supporting information accompanying the benchmark manuscript on (ir)reversible EGFR inhibition by Schwartz and co-worker for a detailed description of Sox substrate kinetics.[93]

Important factors driving EGFR activity observed in PhosphoSens kinase activity assays are the EGFR concentration, the affinity for the Sox-containing substrate (**Figure S4A**), and the concentrations of chelating reagent Mg^{2+} (10 mM) and ATP (1 mM). Additionally, we found that loss of EGFR activity can be minimized by fresh addition of ATP and DTT from single-use aliquots, addition of EGTA to remove Ca^{2+} interfering with Mg^{2+} chelation to CSox substrate,[86] and the use of low-bind tubes. Kinase concentration was optimized to ensure maximum 10% substrate conversion during the measurement (Michaelis-Menten kinetics). The reaction with 0.25 nM GST-EGFR resulted in linear product formation without substrate depletion (less than 10% of the substrate was phosphorylated) for the duration of two hours. A delay in EGFR activity was sometimes observed, probably because the kinase domain is not preincubated with competing ATP (**Figure S4B**). This lag phase, also reported for other Omnia kinase activity assays,[137-138] was excluded from (kinetic) fits.

A   PhosphoSens Kinase Activity Assay

AQT734
CSox EGFR substrate

EGFR
ATP, Mg^{2+}

ChEF
$\lambda_{ex} = 360 \pm 3$ nm
$\lambda_{em} = 492 \pm 7$ nm

pAQT734
Fluorescent phosphorylated product

B

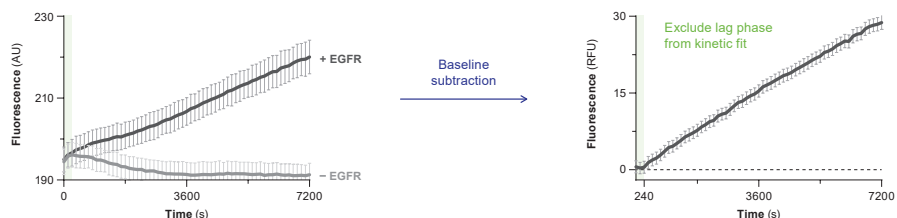Baseline subtraction

Exclude lag phase from kinetic fit

Figure S4 | *In vitro* PhosphoSens kinase activity assay. Data accompanying **Figure 6**. **(A)** EGFR substrate AQT734 is a CSox-based fluorescent chemosensor. CSox is an unnatural amino acid consisting of a cysteine residue alkylated with a sulfonamido-oxine (Sox) with a low intrinsic affinity for Mg^{2+}.[91] Phosphorylation of a nearby tyrosine increases the affinity for Mg^{2+} resulting in a 4-fold increase of chelation enhanced fluorescence (ChEF).[101, 108] **(B)** EGFR activity exhibits a lag phase of ~4 min. This lag phase is excluded from fits after baseline correction (subtraction of signal in CSox substrate in absence of EGFR).

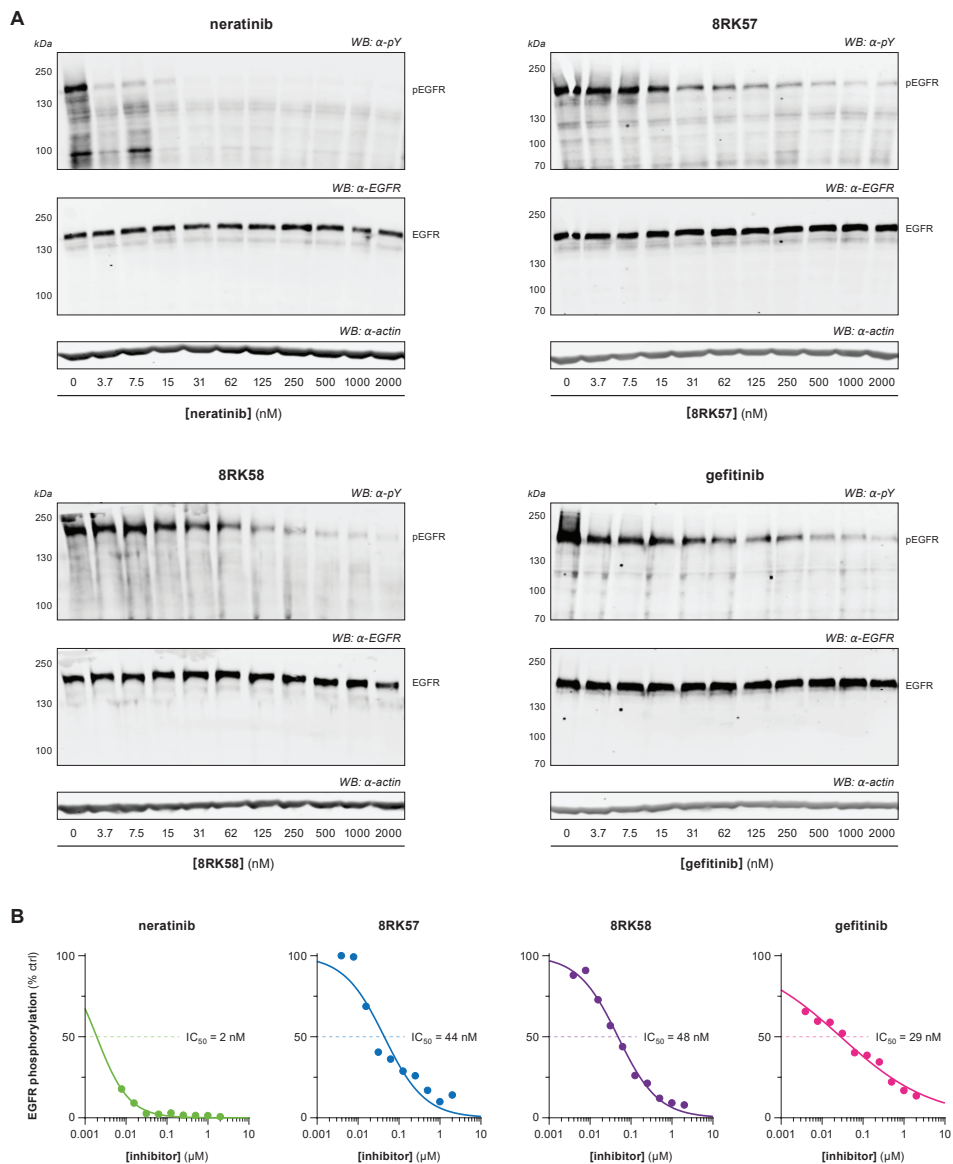## 7.7. Inhibition of Cellular EGFR (Auto)phosphorylation

Figure S5 | Cellular EGFR (auto)phosphorylation in intact HeLa cells. Data accompanying **Figure 7D**. HeLa cells are incubated with various inhibitor concentrations for 1 h. EGFR (auto)phosphorylation is stimulated with EGF (1 h) and receptor (auto)phosphorylation is visualized and quantified from the Western blots. **(A)** Full gel scans. For each inhibitor, phosphorylated tyrosine residues pY *(top)*, total EGFR *(middle)*, and β-actin *(bottom)* are visualized by immunoblotting. Darker bands indicate higher intensity of phosphorylated tyrosine/total EGFR/β-actin. β-actin is a loading control for total protein loading. **(B)** Dose-response curves. Intensity of phosphorylated tyrosine corresponding to pEGFR is divided by intensity of total EGFR, and normalized to the vehicle-treated control. Relative receptor phosphorylation against inhibitor concentration is fitted to the 4-parameter Hill equation to obtain the IC_{50} for inhibition of cellular EGFR (auto)phosphorylation (n = 1).